Gate Controlled InSb Quantum Well and its Application to Resistively Detected Nuclear Magnetic Resonance

Doctoral Dissertation

(博士論文)

Gate Controlled InSb Quantum Well and its Application to Resistively Detected Nuclear Magnetic Resonance

（ゲート制御された InSb 量子井戸とその抵抗検出核磁気共鳴への応用）

Md. Mohi Uddin

Graduate School of Science, Tohoku University

Sendai, Japan

2013

Abstract

Narrow band-gap semiconductor InSb has long been considered as potentially exciting materials for next-generation high-speed, low power electronics and spintronics applications owing to its unique materials properties including high room-temperature mobility (77000 cm^2/Vs) due to small effective mass ($0.014m_e$) and a giant Landé *g*-factor (~ -80 in quantum well) as a result of strong spin-orbit coupling. Silicon-based complementary metal oxide semiconductor (CMOS) scaling is reaching its physical limit to meet Moor's law. The power density (*P*) is getting a serious issue with higher operating frequency and larger integration density in a single chip. *P* can be greatly reduced by using low operating voltage ($P \propto V^2$). The InSb is a strong solution among the III-V semiconductors, because it has very high carrier velocity at low electric field, which means the transistors can maintain high performance at low operating voltage, using reduced power. Moreover, strong spin orbit coupling of the InSb is particularly appealing for spintronics applications, for instance electron spin manipulation in a spin field-effect transistor (spin-FET). A good gate controllability of InSb QW is essential for these device applications.

High nuclear-spin isotopes In ($I = 9/2$) and Sb (^{121}Sb $I = 5/2$, ^{123}Sb $I = 7/2$) and a giant Landé *g*-factor of the InSb have attracted renewed attention for nuclear-spin based measurement and quantum information processing (QIP). By taking advantage of a large *g*-factor in the tilted magnetic field configuration, successful resistively detected nuclear magnetic resonance (RDNMR) has been demonstrated in the quantum Hall ferromagnet (QHF) using a single InSb two dimensional electron gas (2DEG). This achievement is exposed the door to extend the semiconductor materials system for nuclear-spin based measurements and nuclear-spin electronics applications other than well studies GaAs. Gate controlled InSb QW is required to uncover the properties of the electron spins in the QHFs by measuring nuclear-spin relaxation time T_1 at different filling factors. Additionally, control and detection of multiple quantum coherences of nuclear-spins in a nanoscale region such as quantum point contact (QPC) by all-electrical means also entail a gate controlled InSb QW for future QIP. However, experiments have so far been limited because of difficulty to deposit a high quality insulating film on the InSb QW.

The purposes of this study are to fabricate high quality top gated InSb QWs with atomic layer deposited (ALD) Al_2O_3 gate dielectric and investigation of temperature dependent T_1 at different filling factors (ν) using precise pump and probe technique.

We have successfully fabricated gate controlled InSb QWs using atomic layer deposition (ALD) grown Al_2O_3 as a gate dielectric. The density of two dimensional electron gas (2DEG) in the QW is efficiently tuned by gate voltages (V_g) thanks to the good interface of Al_2O_3/InSb, but saturates at large negative V_g. This triumph allows us to study the importance of the layer sequence in gate controllability. At large negative V_g, the valence band (VB) touches the Fermi level (E_F) due to the narrow band gap of top surface layer (InSb) of the QW results the hole accumulates at the surface of the QW and screens the external gate electric field, which has been elucidated by a self-consistent Schrödinger-Poisson (SP) simulation. Accordingly, the 2DEG is not completely depleted in such a QW. Based on the SP simulation, we predict that the 2DEG would be depleted in an InSb QW with a wider-band-gap $Al_xIn_{1-x}Sb$ surface layer that is expected to prevent the hole accumulation by keeping the VB far from the E_F.

We have revealed experimental evidence that the 2DEG is completely depleted in the QWs with a wider-band-gap ($Al_{0.1}In_{0.9}Sb$) surface layer. The interface of Al_2O_3/$Al_{0.1}In_{0.9}Sb$ shows a very weak pinning of the E_F that ensures complete depletion of the 2DEG by application of a small gate voltage (~ -0.9V). This is also reflected by excellent gate controllability with a linear, sharp, and almost hysteresis free behavior in the InSb QWs with wider-band-gap ($Al_{0.1}In_{0.9}Sb$) surface layer. This achievement paves the way to fabricate split-gate defined InSb nanodevices (e.g., QPC).

The success of gate controlled InSb QWs allows us to perform pump and probe technique to investigate the properties of electron spins configuration at the quantum Hall ferromagnet (QHF) by measuring temperature dependent T_1 at different filling factors. Collective spin excitations in the domain walls enhance DNP in the QHF around filling factor $\nu = 1.86$ characterized by a short (~ 60 sec) and temperature-independent T_1. On the other hand, relatively long (~ 400 sec) and temperature dependent T_1 with following Korringa law have been demonstrated in the absence of the domains as well as collective spin texture at around $\nu = 3$. Collective nature of the QHF at the Landau level crossing around $\nu = 2$ has been confirmed in this experiment. In addition, the large Zeeman, cyclotron and exchange energy scales of the InSb 2DEG favor to demonstrate the RDNMR signal at elevated temperature up to 6 K. Our results clearly show that the InSb 2DEG is a suitable candidate for implementation of the high temperature nuclear-spin based QIP.

Acknowledgements

All the glory goes to my creator, the most sympathetic and beneficial who has given me the ability to submit this thesis in partial fulfillment for degree of Doctor of Philosophy.

I am highly obliged to my supervisor Professor Yoshiro Hirayama, and would like to pay my deepest respect and gratitude. His valuable suggestions, understanding and patience, has been of priceless throughout my graduation. He prudently read this manuscript and helped with all the necessary modifications.

My sincere appreciation goes to Professor Hongwu Liu, for his expertise, tireless suggestions, attention to details and informative discussions all through my graduate research. I have benefited a lot from his continuous inspiration.

I express my sincere thanks to Professor Shozo Suto, Professor Katsumi Tanigaki, Professor Atsushi Tsukazaki, and Professor Satoshi Sasaki for being my thesis examiners. I am grateful to my present and former lab members including Mr. Katsumi Nagase for help in the fabrication of most of the devices used in this thesis, Dr. Kaifeng Yang and Dr. Katsushi Hashimoto for continues encourage throughout my graduate research.

I am also grateful to the Institute for International Advanced Research and Education (IIARE) at Tohoku University for their *S-SDC* fellowship during my graduate study. I am thankful to my job institute Chittagong University of Engineering and Technology (CUET) for the study leave to complete my graduation at Tohoku University.

I must acknowledge my beloved mother Mrs. Hosney Ara Begum and remember my father Abdur Rahim for their stimulation and gilding me into the man I am today. I am also thankful to my brothers, father in law, mother in law, my friends and well-wishers for giving me all kind of support.

I am really grateful to my wife for her expenses, support and keeping me free from family affairs during my research work, without it would not have been possible to complete this thesis. Finally, I would like to thank my daughter Faoziya Nusaiba for bringing happiness and joy into our lives.

To my mother Mrs. Hosney Ara Begum

&

To the memory of my beloved father Mr. Abdur Rahim

Contents

List of Figures

List of the Tables

Chapter 1

Introduction

1.1 Motivation

The typical narrow band-gap semiconductor InSb among the III-V compound semiconductors [obtained by combining group III elements (mainly Al, Ga, In) with group V elements (mainly P, As, Sb)] has long been considered as potentially exciting materials for next-generation high-speed, low power electronics [1-3] and spintronics applications owing to its unique materials properties including high room-temperature mobility (77000 cm^2/Vs) due to small effective mass ($0.014m_e$) and a giant Landé *g*-factor (~ -80 in quantum well) as a result of strong spin-orbit coupling. Table 1.1 shows comparison of some significant properties of well studies GaAs and InSb semiconductor systems with respective application fields (red dash circles) [4-14].

	E_g at RT (eV)	Electron mass (m*)	Mobility at RT (cm^2/Vs)	Spin-orbit coupling	Electron *g*-factor	Nuclear spin (*I*)	Mobility at LT (cm^2/Vs)	QHF forms
GaAs	1.42	0.067 m_0	8500	Ω_R= 5 meV A° Ω_D= 31 eV A°³	-0.44	Ga, As = 3/2	36 × 10^6	ν=2/3
InSb	0.17	0.014 m_0	77000	Ω_R= 30 meV A° Ω_D= 490 eV A°³	-80	In=9/2, Sb =5/2, 7/2	0.3 × 10^6	ν=2

Next-generation high-speed and low power electronics

Spintronics applications (spin-FET)

Nuclear spin based measurements & Quantum information processing (QIP)

Silicon-based complementary metal oxide semiconductor (CMOS) scaling is reaching its physical limit to meet Moor's law. The power density (*P*) is getting a serious issue with higher operating frequency and larger integration density in a single chip. *P*

can be greatly reduced by using low operating voltage ($P \propto V^2$). The InSb is a strong solution among the III-V semiconductors, because it has very high carrier velocity at low electric field (as shown in Table 1.1), which means the transistors can maintain high performance at low operating voltage, using reduced power. Moreover, strong spin orbit coupling of the InSb is particularly appealing for spintronics applications, for instance electron-spin manipulation in a spin field-effect transistor (spin-FET) [15]. A good gate controllability of InSb QW is essential for these device applications.

Nuclear-spins in semiconductors are a plausible candidate for future scalable quantum bits (qubits) application due to its very long coherence time. Concomitantly, electron-spin is one of good runners toward qubits because of larger magnetic moment than nuclear-spin by over three orders of magnitude that makes it frank and fast control through magnetic resonance. However, coherent manipulation of electron-spins is strongly affected by background fluctuations in nuclear-spin polarization in nuclear-spin-rich semiconductors, consequently coherence time becomes short. On the other hand, the nuclear-spins retain quantum mechanical properties for extended periods without being influenced by the surroundings. Therefore, precise control of nuclear-spins is required for further implementation of spin-base quantum information processing (QIP). High nuclear-spin isotopes In (I = 9/2) and Sb (^{121}Sb I = 5/2, ^{123}Sb I = 7/2) and a giant Landé g-factor of the InSb (as shown in Table 1.1) have attracted renewed attention for nuclear-spin based measurement and quantum information processing (QIP).

The conventional nuclear magnetic resonance (NMR) technique has been widely used in chemical analysis, physical measurements and medical diagnosis using ^{1}H and ^{13}C nuclei with nuclear-spin I =1/2. In this technique, a tiny shift in the Larmor frequency arises from the surrounding condition can be detected, therefore the NMR operates as a powerful tool for detecting the chemical-bond and electron-spin information surrounding nuclear-spins. However, the conventional NMR has been suffered by a serious drawback, the necessary for a large volume, for example, we need

hundred multiple-layer quantum wells to detect a clear NMR signal with highest sensitivity and sufficient signal-to-noise ratios. Accordingly, it is obviously not suitable for the QIP as well as NMR studies of semiconductor systems. This technological challenge has been recently answered using a highly sensitive resistively detected NMR (RDNMR) based on a single quantum well or nanostructures by means of hyperfine interaction between electron and nuclear-spins.

The RDNMR has been widely used to detect dynamic nuclear polarization (DNP) in the GaAs two dimensional electron gas (2DEG) more than last two decades due to small Landé *g*-factor (-0.44) and high mobility at low temperatures [16-21]. By taking advantage of a large *g*-factor in the tilted magnetic field configuration, successful resistively detected nuclear magnetic resonance (RDNMR) has been demonstrated to study DNP in a single InSb 2DEG [22, 23]. This achievement is exposed the door to extend the semiconductor materials system for nuclear-spin based measurements and nuclear-spin electronics applications other than well studies GaAs. However, filling factor dependent nuclear-spins polarization or their relaxation time T_1 have not been investigated in these studies due to lack of gate controlled InSb QWs. Control and detection of multiple quantum coherences of nuclear-spins in a nanoscale region such as quantum point contact (QPC) by all-electrical means [16] also entail a gate controlled InSb QW for future QIP. Nevertheless, experiments have so far been limited because of difficulty to deposit a high quality insulating film on the InSb QW.

We present our works in this thesis with two parts based on the requirements discussed overhead; fabrication of a gated InSb QW, and its application to the RDNMR to study temperature dependent T_1 time at different filling factors.

Gate controlled InSb QWs

The application of back gate or Schottky contact to the InSb QW is challenging due to a large conductance and high-density dislocation of the buffer layer between the QW and the substrate or low barrier heights. By taking account of these points, top gating with gate dielectrics is expected to be feasible for fabricating the gated InSb QW. Atomic layer deposition (ALD) has been extensively used to grow high-quality high-k dielectrics on the quantum structures of III-V compound semiconductors (GaAs, InAs, GaN, GaSb, etc.) [24]. A few studies have been carried out so far for InSb because of the problem in growing high quality gate dielectric on (Al)InSb and in interfacing dielectric/(Al)InSb [10, 25]. We have successfully fabricated top gate on the InSb QWs with an excellent gate controllability using the ALD techniques.

Resistively detected nuclear magnetic resonance (RDNMR) in gated InSb QW

The RDNMR has been demonstrated in a single InSb 2DEG for the high-nuclear-spin isotopes of In (I = 9/2) and Sb (^{121}Sb I = 5/2, ^{123}Sb I = 7/2) [22]. Information of nuclear and electron-spins configuration as well as their interaction at different filling factors (ν) by means of nuclear-spin relaxation time $T_{1,}$ is essential for further understanding of the dynamic nuclear polarization (DNP) mechanism. We have demonstrated temperature dependent T_1 time at different filling factors in gated InSb QWs by using precise pump and probe technique.

1.2 Scope and organization of dissertation

We study temperature dependent nuclear-spin relaxation time at different filling factors in gated InSb QWs. Precisely, first part of this dissertation is focused on the fabrication of a high-quality top gated InSb QW using ALD technique. Second part is to study

nuclear-spin relaxation time T_1 by using gated InSb QW. Therefore, rest of the dissertation is organized as follows.

Basic concepts of physics related to the 2DEG and the quantum Hall effect (QHE) will be discussed in *chapter 2* as well as notions of the Hall effect, Landau levels and origin of Shuvinikon-de Haas oscillations. Dynamic nuclear polarization via hyperfine interaction and its detection by using novel and highly sensitive RDNMR will be discussed. Basics and process of pump and probe technique to investigate nuclear-spins relaxation at different filling factors will also be discussed. Theoretical concept of a self-consistent Schrödinger and Poisson (SP) simulation and two carrier model to calculate band profile and analyse of parallel conduction channel, respectively will be discussed.

Growth and fabrication of devices will be briefly discussed in *chapter 3*. Mechanism of atomic layer deposition (ALD) as well as slight about dilution refrigerators will also be discussed.

We will show in *chapter 4*, gate controllability of the InSb QWs strongly depends on the layer structure of the QW. We propose the QW layer structure for good gate controllability.

Complete depletion of the InSb 2DEG and excellent gate controllability in the gated InSb QWs with higher band gap surface layer will be discussed in *chapter 5*. Analysis of the interface between the ALD film and the surface layer will also be presented.

Temperature dependent nuclear-spin relaxation time T_1 at different filling factors and high temperature RDNMR up to 6 K will be discussed in *chapter 6*. The results will be elucidated by the existence of collective spin texture in the quantum Hall ferromagnet (QHF).

We will summarize our results and discuss further study in *chapter 7*. Our findings about memory effect in gated InSb QWs at low temperature even at elevated temperatures and gate stability check will also be presented in appendix A and B, respectively. Bibliography and publications with presentations related to this dissertation will be presented at the end of the dissertation.

Chapter 2

Background

2.1 Heterostructure

Heterostructure is formed from heterojunction. If a thin layer of narrower-band gap material is sandwiched between two layers of a wider-band gap material, then they form a double heterojunction. If narrower-band gap material in a double heterojunction is sufficiently thin for quantum properties to be exhibited, then such a band alignment is called a *single quantum well (QW)*. Fig. 2.1 shows a single InSb QW structure, where narrow band gap (InSb) is sandwiched with higher band gap barrier layers ($Al_{0.1}In_{0.9}Sb$).

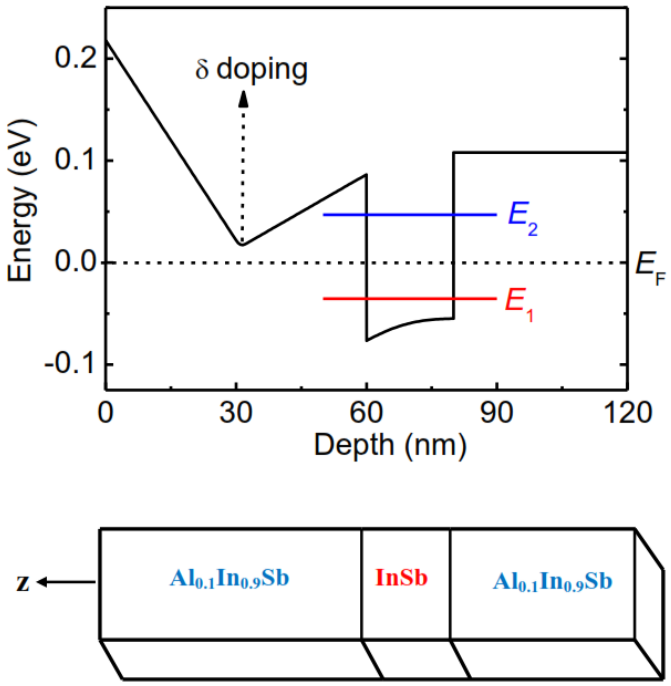

Fig. 2.1: Conduction band profile of a 20 nm-wide InSb quantum well with barrier layers $Al_{0.1}In_{0.9}Sb$ at temperature 2 K. A silicon δ-doping is placed at 30 nm above the QW to provide the electrons to the well and also for surface state. Lowest two energy levels are represented with respect to the Fermi level E_F.

Electrons are free to move in a bulk semiconductor in all direction (3D), their energy above the conduction-band is continuous as represented by *E-K* relationship,

$$E^{3D}(k) = \frac{\hbar^2}{2m^*}\left(k_x^2 + k_y^2 + k_z^2\right) \quad (2.1)$$

where k_x, k_y, k_z denote the wave numbers in x, y, z directions and m^* is the carrier effective mass.

If a carrier is confined in low dimensional systems, such as a quantum well (QW), quantum wire or dot, whose size is comparable with the de-Broglie wave length of an electron, the properties of such electrons as well as their density of state (DOS) exhibit quantum mechanical effects. In QW system, carriers are confined in the growth (z) direction. Owing to a parabolic approximation, the energy in a QW or 2D system changes from (2.1) to:

$$E^{2D}(k) = E_{z,n} + \frac{\hbar^2}{2m^*}\left(k_x^2 + k_y^2\right) \quad (2.2)$$

The eigen energy of a carrier in the QW is comprised of a continuous part, $\frac{\hbar^2}{2m^*}\left(k_x^2 + k_y^2\right)$ defines that the carriers are free to move in the $x-y$ directions and a discrete part, $E_{z,n}$ describes quantized energy level due to confinement potential in the z-direction. Subscript n denotes the number of subbands in the QW. Position of the energy levels in the QW with respect to the E_F depends on the density of states.

The density of states of a semiconductor is defined as the number of states per unit energy per unit volume. It is useful to understand the application of the electronics properties and the experimental study. It depends on the dimension of a system as shown in Fig. 2.2. In a three-dimensional (3D) system, the carrier eigenenergies have a continuous distribution that starts at the band edge (0 eV), and the density of states increases as the square root of the energy [26, 27],

$$\rho^{3D}(E) = \frac{\left(2m^*/\hbar^2\right)^{\frac{3}{2}}}{2\pi^2}\sqrt{E}$$

In a two-dimensional case (QW), the first subband shifts to higher energy due to the quantum confinement effect, consequently the DOS remains zero below the first subband, jumps to a finite constant value until the next subband is reached. Overall it is a series of step functions as a function of energy. For the whole conduction band, the density of states is given by:

$$\rho^{2D}(E) = \sum_{n_z} \frac{m^*}{\pi\hbar^2 L_z}\,\theta\left(E - E_{n_z}\right)$$

Where L is the well width along z -direction, E is the energy relative to the band edge, and $\theta\left(E - E_{n_z}\right)$ is a step function, $\theta(E \geq 0) = 1$ and $\theta(E < 0) = 0$. In real two dimensional electron system, electrons move in the *x-y* plane and length of the quantum well in z-direction can be neglected [i.e., in (m^{-2}) unit]. So, the DOS of each subband takes on the constant value, $\frac{m^*}{\pi\hbar^2}$. The total DOS is the sum over all subbands and is given by:

$$D(E) = \sum_i \theta(E - E_i)\frac{m^*}{\pi\hbar^2}$$

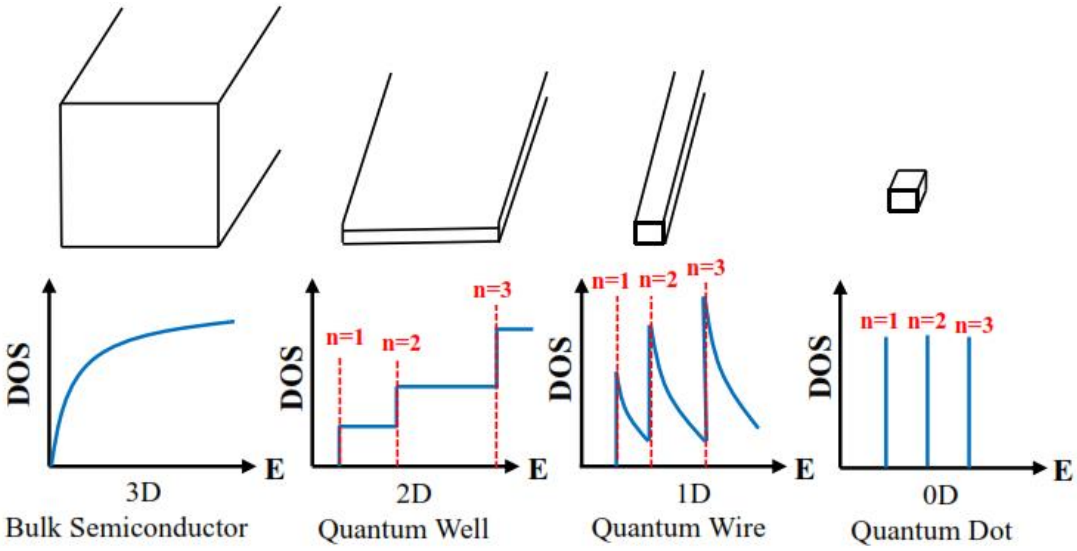

Fig. 2.2: The electronic density of states (DOS) of typical 3D, 2D, 1D, and 0D systems.

For one-dimensional (quantum wire) case, the DOS has an energy dependence which follows $E^{-1/2}$ for each subband. The first subband follows the form:

$$\rho^{1D}(E) = \sum_{n_x,n_z} \frac{(m^*/2\hbar^2)^{1/2}}{\pi L_x L_z} \frac{1}{\sqrt{E-E_{n_x}-E_{n_z}}}$$

In zero-dimension (quantum dot), the momentum of the electrons is confined in all directions and states are only allowed at certain discrete energy values. The DOS follows a series of delta functions:

$$\rho^{0D}(E) = \sum_{n_x,n_y,n_z} \frac{1}{L_x L_y L_z} \delta\left(E - E_{n_x} - E_{n_y} - E_{n_z}\right)$$

where δ is a delta function.

2.2 The Hall effect

In the Hall measurement, electrons are accelerated with drift velocity v_x through a rectangular 2DEG of width W by a current flow along the x-direction ($I_x = env_xW$) in a magnetic field perpendicular to the surface (B_z, with the z-axis the nominal growth direction) as shown in Fig. 2.3.

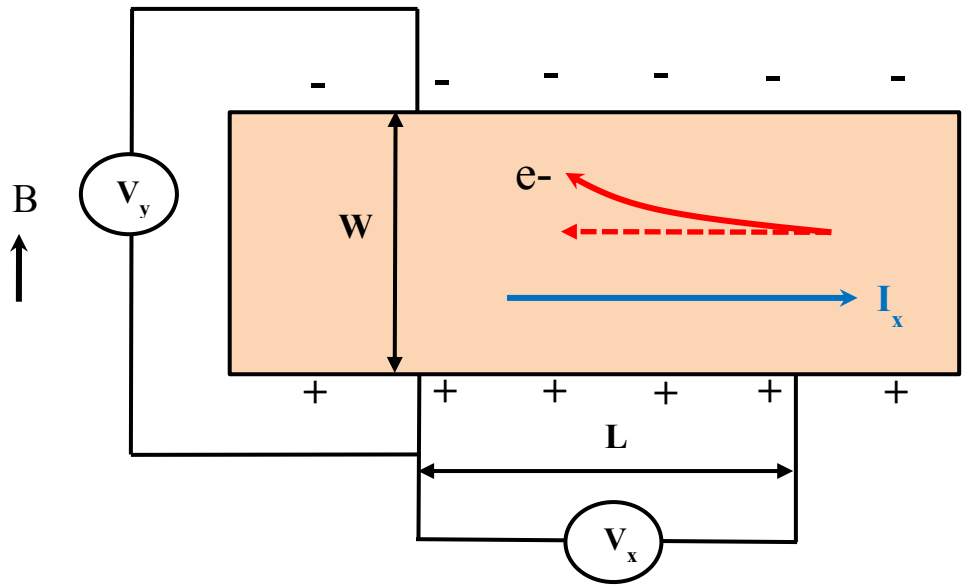

Fig. 2.3: The Hall effect measurement setup, showing the measurement of the voltage dropped longitudinal (V_x) and the Hall voltage (V_y).

The electrons feel a Lorentz force in y-direction $\bar{F} = (e\,\bar{v} \times \bar{B}) = ev_x B_z \hat{\boldsymbol{j}}$ perpendicular to the direction of the current and follow the curved arrow as shown in Fig. 2.3. After a short time, electrons pile up on the upper side and deplete from the lower side which creates an electric filed E_H (V_y/W). This electric field results in a force opposing the Lorentz force, $\bar{F} = e\bar{E} = eV_y/W$. In steady state, E_H creates strong enough force to exactly cancel out the Lorentz force, therefore electrons follow the straight dashed arrow as shown in Fig. 2.3. This allows the carrier density of the 2DEG to be calculated:

$$ev_x B_z = eV_y/W$$

$$n = B_z I_x/eV_y = B_z/eR_H \tag{2.3}$$

where R_H is called the Hall resistance. The resistivity of the 2DEG (ρ_{xx}) can be found from the voltage drop along the side of the 2DEG: $\rho_{xx} = R_x\, W/L$, where $R_x = \frac{V_x}{I_x}$. The resistivity ρ_{xx} and carrier density of the electrons are used to calculate the mobility of the electrons:

$$\mu = 1/en\rho_{xx} \tag{2.4}$$

In this classical measurement, the longitudinal resistance R_x is independent of magnetic field and the Hall resistance R_H is linear with B_z. Therefore, these parameters can't explain the Shubinikov-de Hass oscillations in R_{xx} and the Hall plateaus in R_{xy} in high magnetic field regime at low temperature. We will describe related phenomena to explain such kind of problems in the following sections.

2.3 Landau levels

When a strong magnetic field is applied normal to the heterointerface, the continuous energy spectrum in the two dimensional electron system (2DES) becomes discrete

because of the complete quantization in the orbital motion, and turns into a series of perfectly quantized levels known as Landau levels. The orbital movement of the electrons are defined by the Schrödinger equation:

$$\frac{(-i\hbar\nabla - e\boldsymbol{A})^2}{2m^*}\,\phi\,(x,y) = E\,\phi\,(x,y) \tag{2.5}$$

where $\boldsymbol{A}$ is the vector potential of the magnetic field, with $\boldsymbol{B} = \nabla \times \boldsymbol{A}$. Assuming the Landau gauge, $\boldsymbol{A}\,(x,y,Z) = \left(0,\ B_{x,}0\right)$, and because $\left[P_y\ ,H\right] = 0$. The wave function can be written as:

$$\phi\,(x,y) = \frac{e^{ik_y y}}{\sqrt{L_y}}\,\varphi\,(x) \tag{2.6}$$

By using equation (2.6) into (2.5), an effective one-dimensional Schrödinger equation can be presented:

$$\left[-\frac{\hbar^2}{2m^*}\frac{d^2}{dx^2} + \frac{1}{2}\,m^*\,\omega_c^2(x - x_0)^2 + V(x)\right]\phi_{x0}(x) = E\,\phi_{x0}(x) \tag{2.7}$$

where ω_c is the cyclotron resonance frequency, $\omega_c = e\,B/m^*$. x_0 is the centre coordinate, $x_0 = -l_B^2 k$ and l_B is the magnetic length, $l_B = (\hbar/eB)^{1/2}$. The eigenvalues of equation (2.7) are obtained:

$$E_n = \left(n + \frac{1}{2}\right)\hbar\omega_c, \text{ where } n = 0, 1, 2, \ldots\ldots\ldots\ldots \tag{2.8}$$

where n denotes the index of the Landau levels. Each state is degenerate with respect to x_0. The Landau levels energies are represented by the equation 2.8.

The number of allowed states per unit area is:

$$n_L = \frac{1}{2\pi l_B^2} = \frac{e\,B}{h} \tag{2.9}$$

If an electron has the electron density n_s, the number:

$$\nu = n_s/n_L = hn_s/eB$$

expresses how many Landau levels are occupied at a given magnetic field at zero temperature. Therefore, $\nu = hn_s/eB$ is called the filling factor corresponding to the magnetic field *B*. Electrons are occupied in the Landau levels below the Fermi level (E_F) as shown in Fig. 2.4. External magnetic field changes the energetic separation of Landau levels (cyclotron energy, $\hbar\omega_c$), as well as their degree of degeneracy. Landau levels are lifted gradually with increasing magnetic field *B* and become empty by crossing the Fermi level and corresponding electrons are occupied in the next lower Landau level due to increase degree of degeneracy [28].

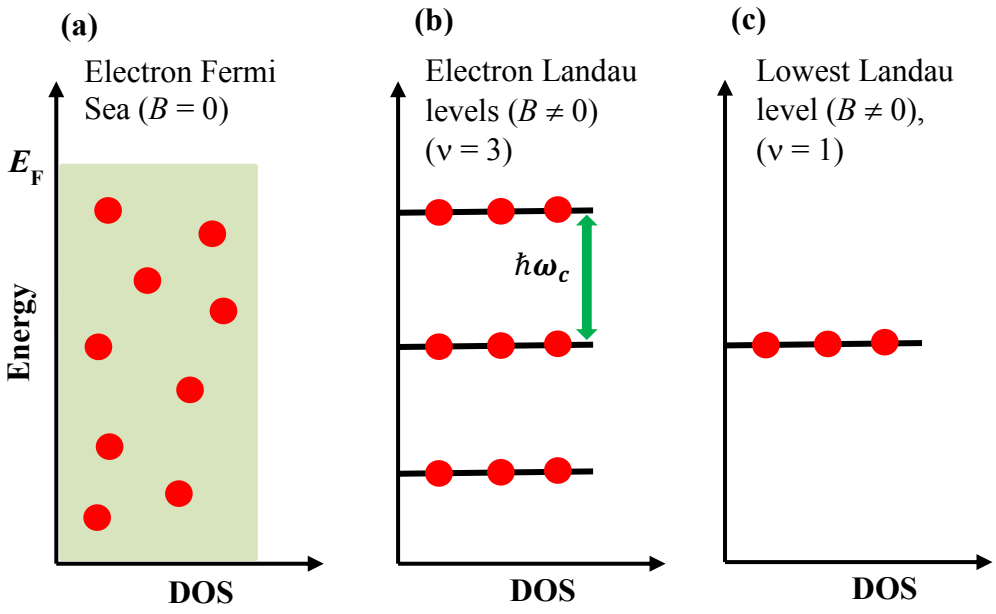

Fig. 2.4: Landau level quantization with increasing perpendicular magnetic field (B).

In real systems, the presence of scattering due to impurities or random arrangement of charged dopants causes broadening of ideal delta shaped density of states (as discussed in section 2.1) peaks into bands (characterised by a broadening parameter Γ) as shown in Fig. 2.5. The centres of the bands are spaced by the cyclotron energy ($\hbar\omega_c$).

There are two types of current carrying state in each Landau level. These can be explained by the thought of Laughlin [29]. A 2DEG in a magnetic field is bent to form a loop (cylinder). The current passes around the loop, with the field perpendicular to the

surface of the loop. The Hall voltage is measured between the ends of the loop. Extended states are continuous around the loop. These are found at the centre of the Landau levels. Localised states are not continuous around the loop and are found at the edges of the Landau levels.

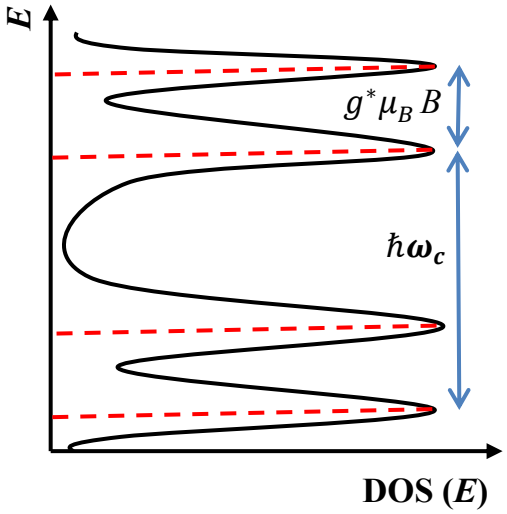

Fig. 2.5: Density of states for electron in a magnetic field. The Landau levels are broadened by scattering with impurities or crystal defects.

The Landau levels are further splitting in a magnetic field. The Zeeman effect is the change in the energy levels resulting from the interaction of the magnetic field on the spin states of the electrons. When we take the Zeeman splitting into account, a further splitting term is added to equation 2.8:

$$E_n = \left(n + \tfrac{1}{2}\right)\hbar\omega_c \pm \tfrac{1}{2} g^*\mu_B B \qquad (2.10)$$

where g^* is the Lande g-factor. The Zeeman splitting results in a splitting of the Landau levels due to lifting of the spin degeneracy of the levels, with $\Delta E^{\uparrow\downarrow} = g^*\mu_B B$ splitting between the levels.

2.4 Shubnikov-de Hass oscillations and the quantum Hall effect

The energy of a given Landau level increases linearly with the magnetic field *B*, leading to the so-called Landau fan which is the energy diagram as illustrated in Fig. 2.6. The number of occupied Landau levels is represented by the filling factor ν (hn_s/eB). At a fixed electron density n_s, the Fermi level of the electron gas oscillates as a function of *B*, i.e., with filling factor ν in a 1/*B* periodic fashion. These oscillations in R_{xx} are known as Shubnikon-de Haas (SdH) oscillations as shown in Fig. 2.7. If the Zeeman splitting $g^*\mu_B B$ is negligible compared to the Landau levels separation $\hbar\omega_c$, each Landau level holds $2eB/h$ electrons per unit area and the Fermi energy jumps between Landau levels at even value of ν.

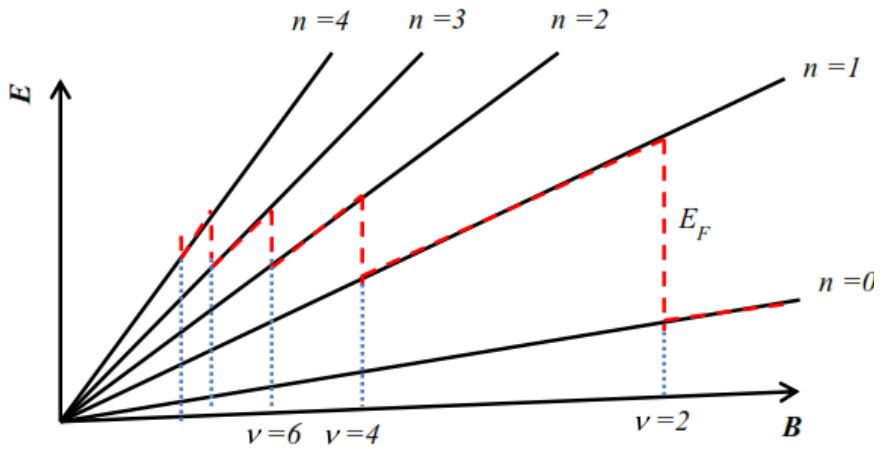

Fig. 2.6: Landau level fan, showing the Fermi level E_F (red line). The slop of the each Landau level line depends on the quantum number *n*.

When the Fermi level lies in the extended states, there are a maximum number of states to scatter into, and so the longitudinal resistivity ρ_{xx} ($\rho_{xx} = R_{xx}\, W/L$, where W and L are the width and length, respectively according to the sample geometry) is a maximum. Away from the Landau levels, scattering is suppressed and so ρ_{xx} falls to about zero as shown in Fig. 2.7. The conductivity σ_{xx} also exhibits maxima when the Fermi level lies in the centre of a Landau level, and minima when it is between levels, i.e., σ_{xx} is proportional to ρ_{xx}. This is because, current and voltage are not collinear in a

magnetic field and therefore conductivity σ and resistivity ρ are no longer inverse to each other, but obey a tensor relationship $\sigma = \rho^{-1}$.

The Hall resistance, R_{xy} shows plateaux ($dR_{xy}/dB = 0$) for a particular magnetic field as shown in Fig. 2.7. Classically, the Hall resistance is given by R_H $(R_{xy}) = B/en$ (as discussed in section 2.3), where n is the number of carriers. In each Landau level, there are eB/h current carrying states. When the number of Landau levels lies below the Fermi level, say ν, then $n = \nu eB/h$, therefore $R_{xy} = \frac{1}{\nu} h/e^2$. The localised states are not continuous around the loop 2DEG (as discussed in section 2.3) they are not affected by the magnetic field [29]. Consequently, when the Fermi level sweeps through the localised states, the Hall resistance does not change. This is known as the quantum Hall effect (QHE). The plateaux occur for $R_{xy} = \frac{1}{\nu} h/e^2$ where ν is an integer for the integer quantum Hall effect as shown in Fig. 2.7 [30, 31].

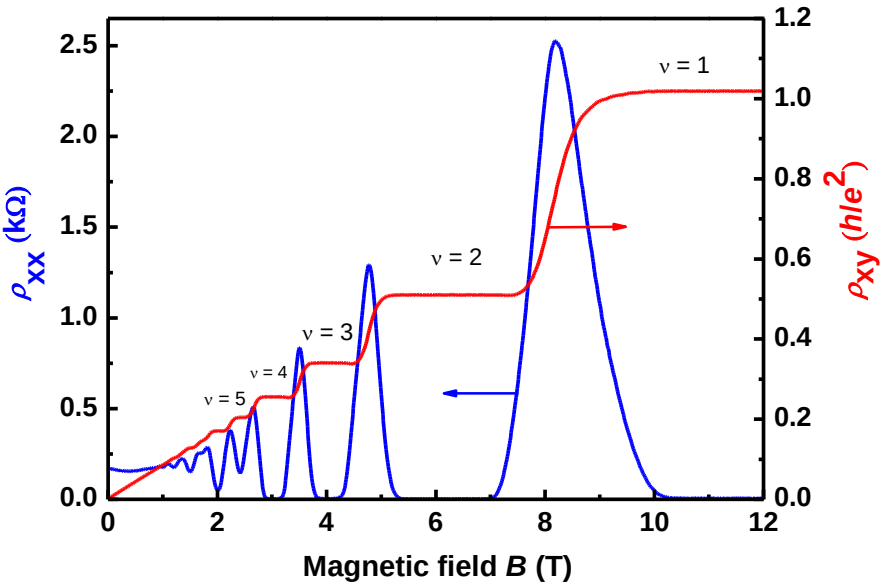

Fig. 2.7: Integer quantum Hall effect in InSb/AlInSb heterostructure with carrier density $n_s = 2.8 \times 10^{15}$ m^{-2} and electron mobility $\mu = 13.0$ m^2/Vs at temperature 2 K. The Hall resistance R_{xy} shows a staircase with the Hall plateau ($\nu = 1, 2, 3, \ldots\ldots$) and diagonal resistance R_{xx} exhibits the Shubnikov-de Hass oscillations, vanishing at Hall plateaus.

We can obtain the two dimensional carrier density n_s and the electron mobility μ from the measured low field resistances R_{xx} and R_{xy} by

$$n_s = 1/e\ (dR_{xx}/dB)^{-1}$$

and $\mu = 1/en_sR_{xx}(0T)$.

Disregarding Zeeman splitting, a Fourier transform of $1/B$ vs R_{xx} will result a frequency f_{SdH} for each subband. The carrier concentration n_s in separate subbands can be determined from f_{SdH} by means of the relation $n_s = (e/h)\ f_{SdH}$.

2.5 Dynamic nuclear polarization (DNP)

Nuclear-spins have attracted less attention in most studies involving semiconductor devices and their physics due to weak coupling between nuclear-spins and conductive electrons. Recently, this situation has been changed when novel nuclear magnetic resonance (NMR) discovered by Berg et al. based on interaction between electron-spin and nuclear-spin in semiconductor heterostructure [32, 33]. Nuclear-spins are dynamically polarized by current flow and their polarization is detected by measuring resistance using transport characteristics. Dynamic nuclear-spin polarization is induced by interaction between nuclear-spin and electron-spin through hyperfine coupling in semiconductors.

2.5.1 Hyperfine Interaction

Hamiltonian of a nuclear-spin in a static magnetic field B_0 is represented [20, 21] by

$$H = H_n + H_Q + H_{HF} \tag{2.11}$$

First term H_n is the Hamiltonian of an isolated nuclear-spin in B_0 and presents by $H_n = \gamma_n \hbar B_0 I_z$, where I_z is the nuclear-spin operator and γ_n is a nuclear gyromagnetic ratio. The second term H_Q is a quadrupolar interaction, comes from strain in the

semiconductor structures. We anticipate in ^{115}In (I = 9/2) in InSb nine equally separated resonances under the certain quadrupolar splitting. The third term H_{HF} arises from mutual interaction between nuclear and electron-spins which is called hyperfine interaction and expressed by [18, 19]:

$$H_{HF} = A_{HF}\, \boldsymbol{I}.\, \boldsymbol{S} \tag{2.12}$$

Here A_{HF} is the hyperfine constant, $\boldsymbol{I}$ is the nuclear-spin and $\boldsymbol{S}$ is the electron-spin.

Equation (2.12) can be expressed by the ladder operator as

$$H_{HF} = A_{HF}\left[\frac{1}{2}\left(\boldsymbol{I}_{+}\,.\,\boldsymbol{S}_{-} + \boldsymbol{I}_{-}\,.\,\boldsymbol{S}_{+}\right) + \boldsymbol{I}_{z}\,.\,\boldsymbol{S}_{z}\right] \tag{2.13}$$

where ladder operators are $\boldsymbol{I}_{+} = \boldsymbol{I}_{x} + i\,\boldsymbol{I}_{y}$, $\boldsymbol{I}_{-} = \boldsymbol{I}_{x} - i\,\boldsymbol{I}_{y}$, $\boldsymbol{S}_{+} = \boldsymbol{S}_{x} + i\,\boldsymbol{S}_{y}$ and $\boldsymbol{S}_{-} = \boldsymbol{S}_{x} - i\,\boldsymbol{S}_{y}$. First two terms present flip-flop process of nuclear and electron-spins and third term expresses Zeeman interaction between nuclear and electron-spins. Nuclear-spin polarization is induced by flip-flop process through hyperfine interaction between nuclear and electron-spins. Although energy-conservation rule is not satisfied

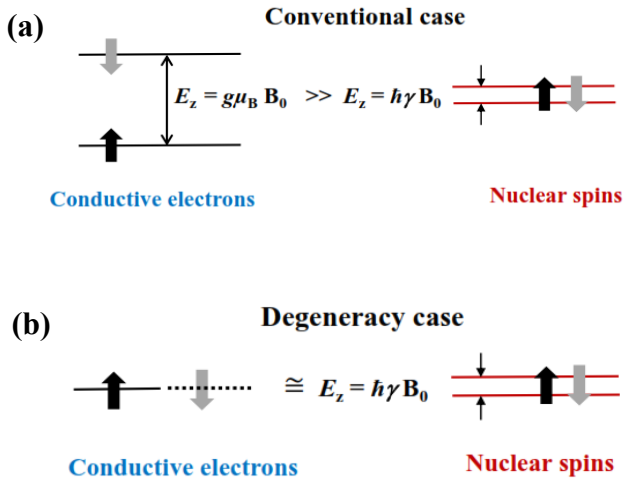

Fig. 2.8: Schematic energy diagram of conductive electron and nuclear-spins under static magnetic field B_0 in conventional case (a) where electron Zeeman energy (E_z) is three order greater than that nuclear-spins and degeneracy case (b) where different electron states with opposite spins degenerate, therefore energy difference between opposite spins close to the nuclear-spin Zeeman energy.

in conventional case resulting weak interaction between electron and nuclear-spins because the Zeeman energy (E_z) between two different electron-spin states is three order magnitude larger than that of nuclear-spin as shown in Fig. 2.8 (a). However, the extremely large g^* of the InSb 2DEG in tilted magnetic field makes a crossing point of Landau levels with different electron-spin states. Therefore, both energy and momentum conservation rules are satisfied and flip-flop process occurs between electron and nuclear-spins as shown schematically in Fig. 2.8 (b).

Electron-spins feel hyperfine field due to the polarization of nuclear-spins and can be represented as

$$\boldsymbol{B}_N = \frac{A_{HF}\langle \boldsymbol{I} \rangle}{g^* \mu_B} \tag{2.14}$$

where $\langle \boldsymbol{I} \rangle$ is the average nuclear-spin. Therefore, Zeeman energy of electrons increases by$g^* \mu_B B_N$, here μ_B is the Bohr magnetron. Electrical or optical characteristics sensitive to this change of Zeeman energy, can be used as a detectors of nuclear-spin polarization.

2.5.2 DNP in quantum Hall ferromagnet (QHF)

Dynamic nuclear polarization (DNP) in QHFs has attracted extensive attention due to its importance to study spin dynamic and spin based quantum information processing [20, 34]. A rich class of magnetic phenomenon in two dimensional electron system (2DES) has recently been subject of intense research due to Landau levels crossing with opposite spin polarizations [22].

Sample with 2DEG rotates around a magnetic field B_{tot} [Fig. 2.9 (a)], coincidence occurs each time the ratio between the Zeeman energy [$E_z = \hbar\omega_s = g^* \mu_B B_{tot} = g^* \mu_B B_\perp / cos\theta$, where μ_B is the Bohr magneton, g^* is the effective electron Lande g factor and θ is the tilt angle] and the cyclotron energy [$E_c = \hbar\omega_c =$

$\hbar eB_{\perp}/m^{*}$, where $\hbar$ is the reduced Planck's constant and m^{*} is the effective mass of the electrons] is an integer $r = E_z/E_c = 1,2, \ldots \ldots$ as schematically shown in Fig. 2.9 (b) [35].

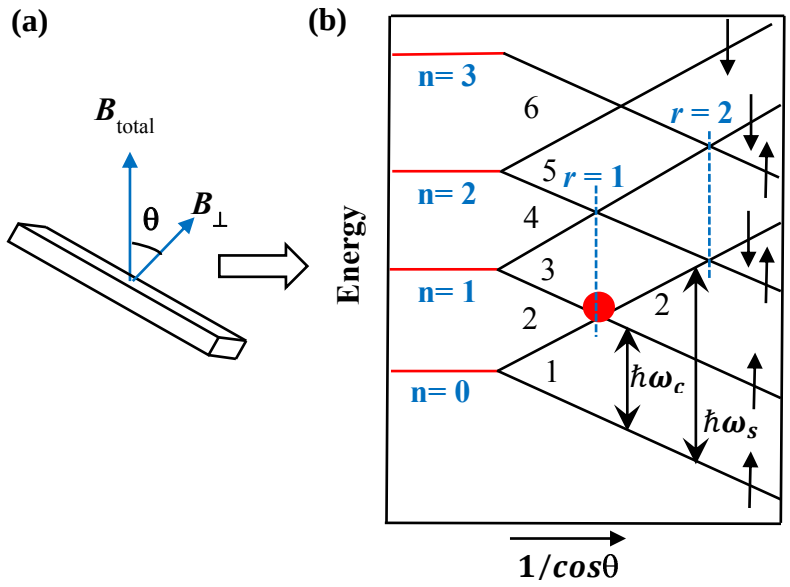

Fig. 2.9: (a) Sketch of a sample in tilt-angle geometry. (b) Schematic diagram of the electron Landau levels with spin-split, spin-up (↑)and spin-down (↓) intersection vs. $1/cos\theta$ (i.e., total magnetic field increases but keeping perpendicular field $B_{\perp} = B_{tot}cos\theta$ or cyclotron energy $\hbar\omega_c$ constant.

At the intersection, Landau level energy gap collapses due to absence of electron-electron interactions results a resistance peak or Landau peak (dashed lines in Fig. 2.10) instead of an R_{xx} minimum. In InSb 2DEG, g^{*} is large (~ -80 in quantum well) [8], therefore the Landau level degeneracy with opposite electron-spin states at easy accessible magnetic field can be achieved due to remarkable enhancement of $\hbar\omega_s$. The spin-down state of the ground Landau level ($n = 0$) and the spin-up state of the first Landau level ($n = 1$) cross each other at $\nu = 2$ and quantum Hall ferromagnet (QHF) formed as indicated by the circle (red) in Fig. 2.9 (b). Here, QHF has easy-axis (Ising) anisotropy and characterized by the resistance spike or spike within persistent longitudinal resistance R_{xx} minima as shown in Fig. 2.10 (red dashed circle). Electrons therein prefer to occupy aligned Landau levels in the ordered state to gain exchange

energy prior to single-particle energy crossover. Disorder or finite temperature, however, may lead to the formation of partially or fully polarized magnetic domains separated by domain walls [36]. In the case of large wall loops, electrons, at coincidence (r), can diffuse along the walls and can thus backscatter from one edge of the Hall bar to the other, giving rise to resistance spikes in the QHF region [36-39]. The exchange energy is expected to be large at the QHF region [37]. Current induced DNP is occurred via flip-flop process between electron and nuclear-spins through hyperfine interaction at the QHF region at around $\nu = 2$ and successfully detected by the RDNMR.

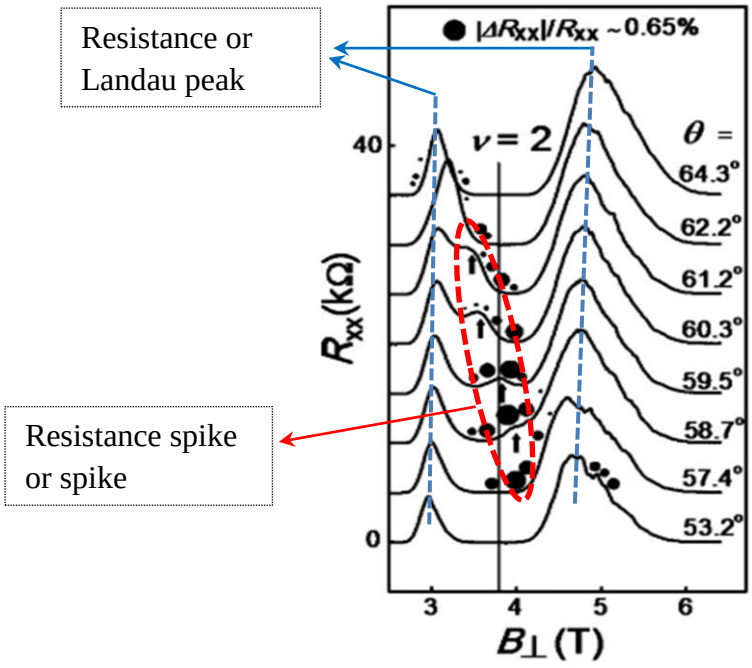

Fig. 2.10: Longitudinal resistance (R_{xx}) vs perpendicular magnetic field ($B_{\perp}$) at different angles θ around ν =2. The θ is the tilt angle as shown in Fig. 2.9 (a). The curves have been offset for clarity. The resistance peaks or Landau peaks (blue) and resistance spikes or spikes (red) are indicated by the dashed lines and circle, respectively. The arrows (inside the red dashed circle) point out distinguishable resistance spikes in the magnetotransport measurement. The dots and their diameter indicate the resistively detected nuclear magnetic resonance (RDNMR) detection regions and the ratio between the RDNMR resistance change $|\Delta R_{xx}|$ of ^{115}In resonance and the R_{xx} value, respectively. Adapted with permission from H. W. Liu *et al.* [22].

2.5.3 Pump and probe technique

Dynamic nuclear polarization process and its detection in the tilted angle geometry have been discussed in the previous section. Gate controlled InSb QW allows us to study nuclear-spins relaxation at different filling factors using pump and probe technique. In this measurement technique, nuclear-spins are polarized under special condition and then system is switched to state of interest which we want to study, say temporal filling factors (ν_{temp}) by using top gate bias. Finally system backs to original condition and detect resistance changes due to nuclear-spin relaxation during $\nu_{temp.}$ We can enjoy nuclear-spin based measurements for any state we need to study by pump and probe experiment [39].

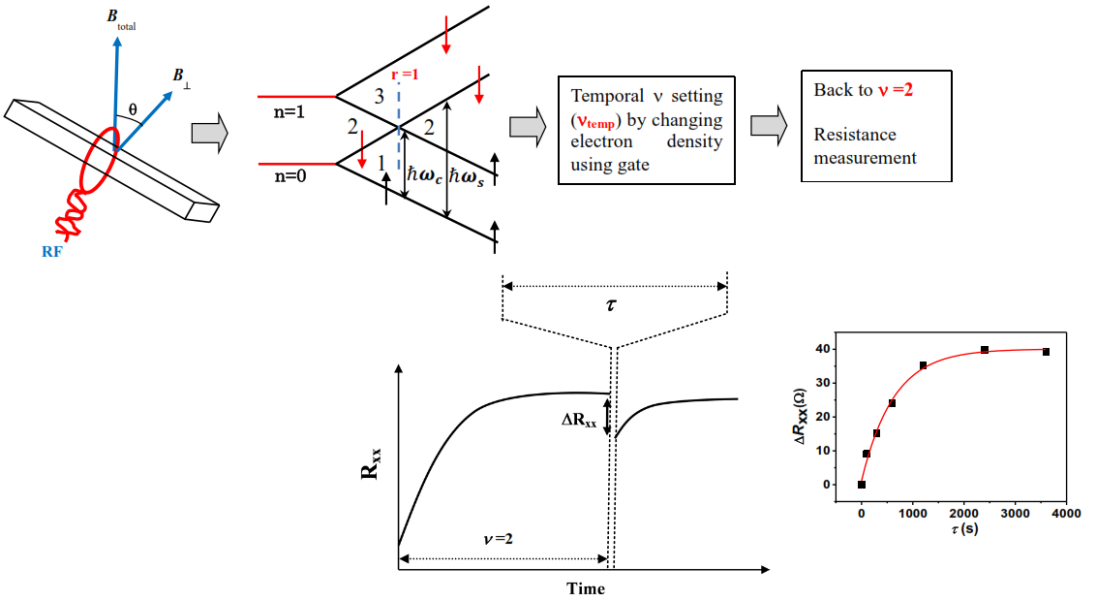

Fig. 2.11: Schematic illustration of nuclear-spin relaxation, T_1 time measurement by pump and probe experiment based on resistance detection of nuclear-spin polarization.

We first polarize nuclear-spins by flowing a large current in the quantum Hall ferromagnet (QHF) around ν = 2 in tilted magnetic field. Peak resistance of the QHF is increased due to the nuclear-spin polarization and becomes saturate after a large current is applied as shown in Fig. 2.11. Sample then set to the temporal filling factor ν_{temp} (nuclear-spin state of interest) for a time interval, say τ by changing gate voltages V_g.

Current is switched off during τ to avoid unintentionally nuclear-spin polarization. Finally, the filling factor is retuned to ν = 2 to measure resistance relaxation (ΔR_{xx}) during the time τ. We measure ΔR_{xx} for several values of τ in same ν_{temp}. The plot of ΔR_{xx} versus τ shows an exponential curve for ν = ν_{temp} as shown in Fig. 2.11. T_1 is calculated by exponential fitting the data to the form $\Delta R_{xx}(\tau) = \Delta R_{xx,s}\left[1 - e^{-\tau/T_1}\right]$, where $\Delta R_{xx,s}$ represents the saturation of ΔR_{xx}.

2.6 Self-consistent Schrödinger and Poisson (SP) solution

The dimensions of electronic devices are approaching to nanometer scale due to the rapid progress in semiconductor technology. The electronic states in confined semiconductor structures such as quantum well are controlled by quantum mechanical size quantization. The physical equations that describe these quantum systems are much too complex to be solved analytically and efficient numerical solution methods need to be used instead. In quantum well, discrete energy levels, the so called energy subbands occur, which is discussed in section 2.3. The electronic subbands of the conduction band and the corresponding envelope functions can be determined by solving the Schrödinger equation self-consistently with the Poisson equation [40].

The formation of 2DEG in a quantum well in a heterostructure is defined as one lower bandgap semiconductor is sandwiched with two higher bandgap semiconductors as shown in section 2.1. When two or more semiconductors sandwiched together, the Fermi levels are reached into equilibrium position with each other. The band of individual layer tends toward its equilibrium position results band bending away from the interface. The electric field is created due to band bending inside the heterostructure and assistances to brought Fermi levels into equilibrium position with each other.

The energy eigenvalues and wave functions are calculated by incorporating the potential due to the carrier density into Schrödinger equation.

$$-\frac{\hbar^2}{2m^*}\frac{d^2}{dz^2}\psi(z)+V(z)\psi(z)=E\psi(z) \tag{2.15}$$

Electrostatic potential $\phi(z)$ is then calculated by Poisson's equation;

$$\frac{d^2}{dz^2}\phi(z)=\frac{\rho}{\varepsilon} \tag{2.16}$$

Where ρ is the charge distribution and ε is the permittivity of the material, i.e., $\varepsilon = \varepsilon_r\varepsilon_0$.

The potential $V(z)$ in equation (2.15) becomes:

$$V(z)=-q\phi(z)+\Delta E_c(z) \tag{2.17}$$

where $\Delta E_c(z)$ is the pseudopotential energy due to the band offset at the heterointerface.

Therefore, it is necessary to form a closed loop for solving Schrödinger equation, calculating the potential due to the resulting charge distribution, adding it to the original band-edge potential, solving Schrödinger equation again, and so on until the update is below a certain limit, thus convergency is reached as illustrated schematically in Fig. 2.12. The conduction band (CB) profile is calculated by a self-consistent Schrödinger and Poisson solution for InSb/AlInSb heterostructure with a 20 nm-wide InSb QW is shown in Fig. 2.13.

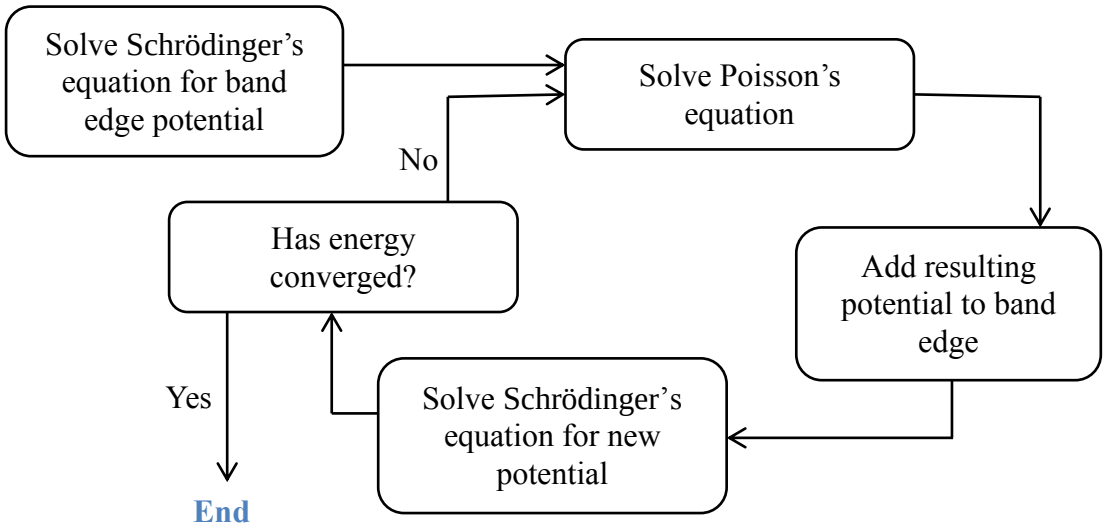

Fig. 2.12: Block diagram illustrating the process of a self-consistent iteration of Schrödinger and Poisson solution.

Temperature dependent band gap E_g is calculated by $E_g(T) = E_g(T=0) - \alpha T^2/T + \beta$, where Varshni parameter for InSb is $\alpha = 0.32\ meV/K$ and $\beta = 170\ K$ [41] and for the alloy $Al_xIn_{1-x}Sb$ can be calculated by $E_g(x) = E_g(0) + (2.0\ eV)x$ [42]. A metal-semiconductor contact is treated as Schottky contact in this calculation. The Schottky barrier height ϕ_B is implemented as Fermi level pinning, where the conduction band edge is pinned with respect to the Fermi level E_F due to the surface state (interface state). In this model barrier height is independent of the metal work function and completely determined by the surface states. Typical Neumann boundary conditions for the Poisson equation are employed which implies a vanishing electric field at the boundaries ($\partial\phi/\partial x = 0$). There is no electric field below the QW, therefore full device is not simulated.

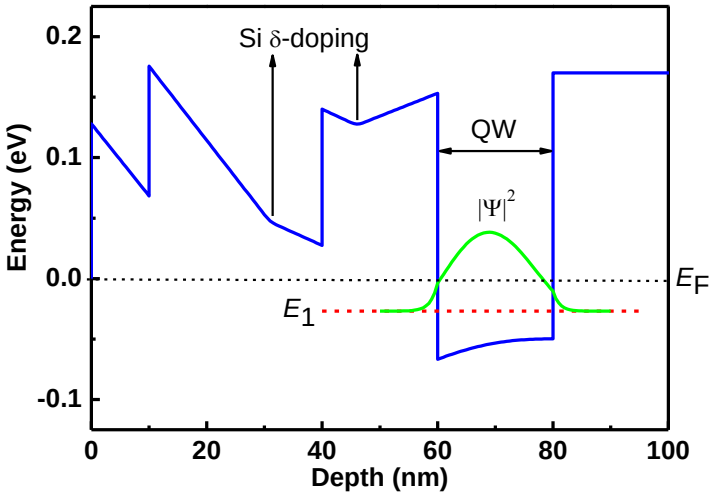

Fig. 2.13: The conduction band profile of InSb/AlInSb heterostructure calculated from a self-consistent Schrödinger-Poisson solution at 2 K (blue line). Lowest energy state (red dashed line) and electron density distribution (green line) in the QW are illustrated. The energy axis is scaled so that the Fermi level lies at 0 eV.

2.7 Theory of two carrier model

A parallel conduction channel emerges in the gated InSb QW due to reducing ϕ_B after the ALD process. Parallel conduction carrier density and mobility can be determined by two carrier model [43]. In the following paragraph, two carrier model will be discussed.

The sheet resistivity tensor ρ_i of a two dimensional layer (i is the subscript of the conducting layer, not one of the components of the tensor) in the presence of a magnetic field is represented as:

$$\boldsymbol{\rho}_i = \begin{pmatrix} \rho_{0_i} & \frac{B}{en_i} \\ \frac{-B}{en_i} & \rho_{0_i} \end{pmatrix} \tag{2.18}$$

where zero field resistivity $\rho_{0_i} = m_i/en_i\tau_i$ and the relaxation time $\tau_i = \mu_i m_i/e$, here μ_i is the mobility, n_i is the carrier density and m_i is the effective mass of the conduction layer.

The total sheet conductivity is the sum of different layers, since total current is the sum of the different layers. The conductivity tensor for *i* layer is inversion of equation (2.18):

$$\boldsymbol{\sigma} = \frac{1}{{\rho_0}^2 + \frac{B^2}{e^2{n_i}^2}} \begin{pmatrix} \rho_{0_i} & \frac{-B}{en_i} \\ \frac{B}{en_i} & \rho_{0_i} \end{pmatrix}$$

$$\text{and} \quad \boldsymbol{\sigma}_{tot} = \sum_i \begin{pmatrix} D_i & -A_i \\ A_i & D_i \end{pmatrix} \tag{2.19}$$

with $D_i = \frac{e^2 n_i}{m_i} \frac{\tau}{1+\omega_c^2\tau^2}$ and $A_i = \frac{e^2 n_i}{m_i} \frac{\omega_c^2\tau^2}{1+\omega_c^2\tau^2}$, where $\omega_c = \frac{eB}{m_i}$ and $\mu = \frac{e\tau}{m_i}$

The sheet resistivity is obtained from inverting equation 2.19. The diagonal and off-diagonal (Hall) resistivity components are related to the conductivity tensor, respectively by,

$$\rho_{xx} = \frac{\sum_i D_i}{\left[(\sum_i D_i)^2 + (\sum_i A_i)^2\right]} \tag{2.20}$$

and

$$\rho_{xy} = \frac{\sum_i A_i}{\left[(\sum_i D_i)^2 + (\sum_i A_i)^2\right]} \tag{2.21}$$

Equations (2.20) and (2.21) provide the information of carrier density and mobility for the conductive channels over the range of magnetic field.

Chapter 3

Materials system and device fabrication techniques

Two dimensional electron gases (2DEGs) form in the InSb quantum wells (QWs) have been the subject of numerous experimental and theoretical studies owing to its unique properties including high intrinsic electron mobility at room temperature due to light effective mass among the III-V semiconductors system. We design different InSb QWs and the aim of this chapter is to introduce QWs used in this study as well as fabrication processes. Our device fabrication process is completed within two steps basically; the first is Hall bar fabrication and the other top gate fabrication using atomic layer deposited (ALD) gate dielectric Al_2O_3. Therefore, we begin the first step with heterostructure design (section 3.1), device geometry, i.e., Hall bar fabrication (section 3.2), mesa etching (section 3.2.2) and ohmic contact in section 3.2.3. We discuss ALD mechanism and preparation for gate deposition as well as our used ALD recipes in section 3.3. Our measurements are performed at extremely low temperature using dilution refrigerator unit, e.g., mK level. Hence, basic concept of cryogenic system is discussed at the end of this chapter.

3.1 Heterostructure design

The RDNMR has been demonstrated in a single InSb QW at around filling factor 2 for the first time other than GaAs among all binary III-V semiconductors system [22]. This discovery of InSb QW brings into spotlight in low temperature fundamental research towards nuclear-spin based quantum bits (qubits) for future quantum information processing. Schematic of our heterostructures used in this dissertation are shown in Fig. 3.1.

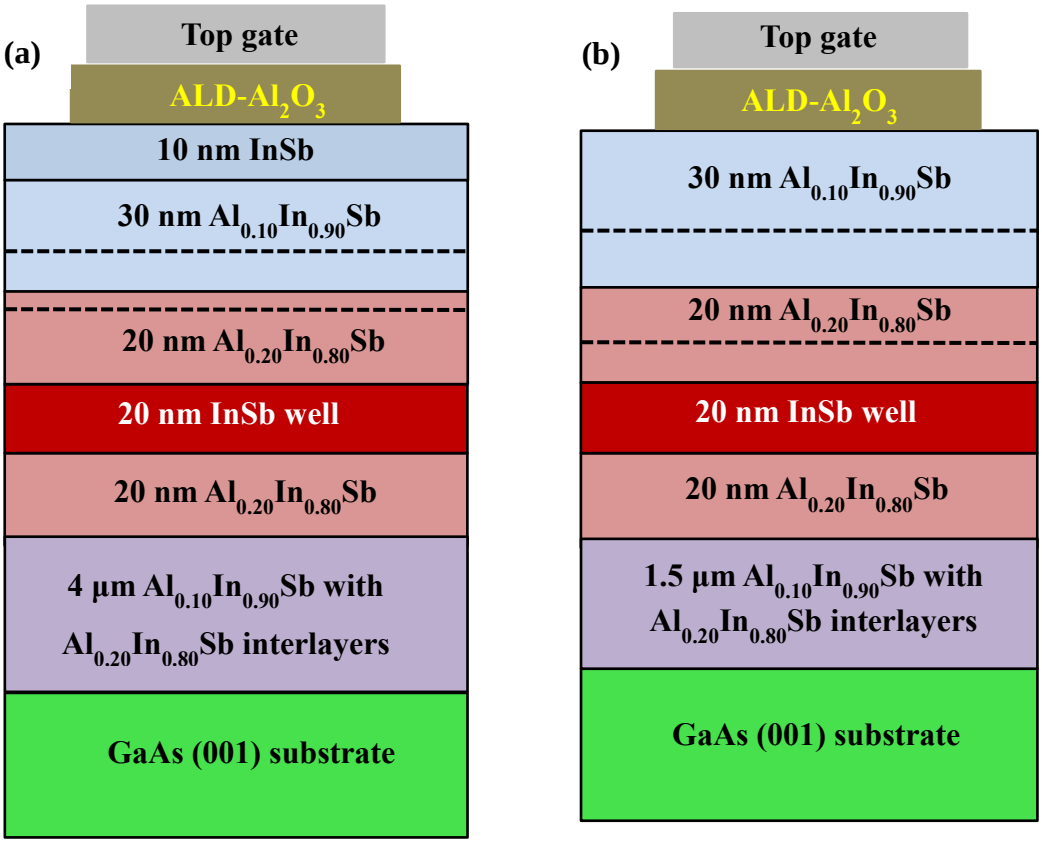

Fig. 3.1: Schematic of our heterostrcutures with different top layers (a) InSb (t335) and (b) $Al_{0.1}In_{0.9}Sb$ (t138). The dashed lines indicate Si δ-doping layer.

The InSb/$Al_xIn_{1-x}Sb$ multilayers were grown on GaAs (001) substrates using an Intevac Modular Gen II molecular beam epitaxy (MBE) system under collaboration with Professor M. B. Santos group at University of Oklahoma [44]. Semi-insulating GaAs (001) (with 2° cut off toward <110>, to enhance reduction of micro twin defect density in the epilayers) [45] has chosen as a substrate for InSb QWs. In spite of its large lattice-mismatched (~14.6%), GaAs thought to be sensible due to its high-quality, availability and reasonable price. InSb QWs growth on lattice-matched InSb substrates is not viable for applications due to its narrow band gap, thereby a large intrinsic carrier concentration at room temperature.

3.2 Sample fabrication

Standard Hall bar geometry with atomic layer deposited (ALD) gate dielectric is used in this study. Dust contamination is one of the problems during nanostructure fabrication, since they produces defects. Therefore we have used clean room under a hood to avoid such kind of contamination. Two major steps are followed to fabricate gated InSb QWs. First, a Hall bar is fabricated using standard photolithography process. Second, gate dielectric is deposited by ALD technique. Details of sample fabrication process are described in the following sections:

3.2.1 Photolithography

Photolithography is the process used to pattern Hall bar fabrication. Schematic of a single photolithography steps is shown in Fig. 3.2. A piece of heterostucture wafer (hereafter referred to as "samples") is cut by a diamond cutter. The samples are cleaned in acetone, Isopropyle (IPA), de-ionized water (DIW) followed by nitrogen gas blown dry to remove unexpected matter on the surface. The samples are then dehydration bake at 110°C (5 min) in a conventional oven before the spin coating process. The samples are positioned on a spinner chuck by vacuum and places S1813G positive photoresist drops on the sample surface. Photoresist thickness depends on the spinning speed and viscosity of the solution. Spinner rotates at low speed 500 rpm (3sec) and high speed 4000 rpm (40 sec) to achieve desired thickness of the resist. The samples are then soft bake at 110°C (5 min) in an oven to evaporate excess photoresist solvents during the spin coating process and photoresist becomes photosensitive.

The samples are placed on the surface of MIKASA MA-20 *mask aligner*, a device designed for aligning and adjusting the sample with respect to a mask. The "photomask" is a square glass plate with a Hall bar mesa patterned (Fig. 3.3) emulsion of metal film on one side. Ultraviolat (UV) light is then exposed through the pattern in the mask on the photoresist with a high intensity for 12 sec from 300 W UV source as shown

schematically in Fig. 3.2. The Hall bar pattern is developed in MICROPOSIT 351 developer solution for 40 sec followed by clean with DIW and blown with dry nitrogen jet. A post bake at 110°C for 20 minutes is then employed to evaporate excess solvents produces from the development process. An O_2 plasma etching with power 20 W (10 sec) is employed to oxidize photoresist and facilitates its removal.

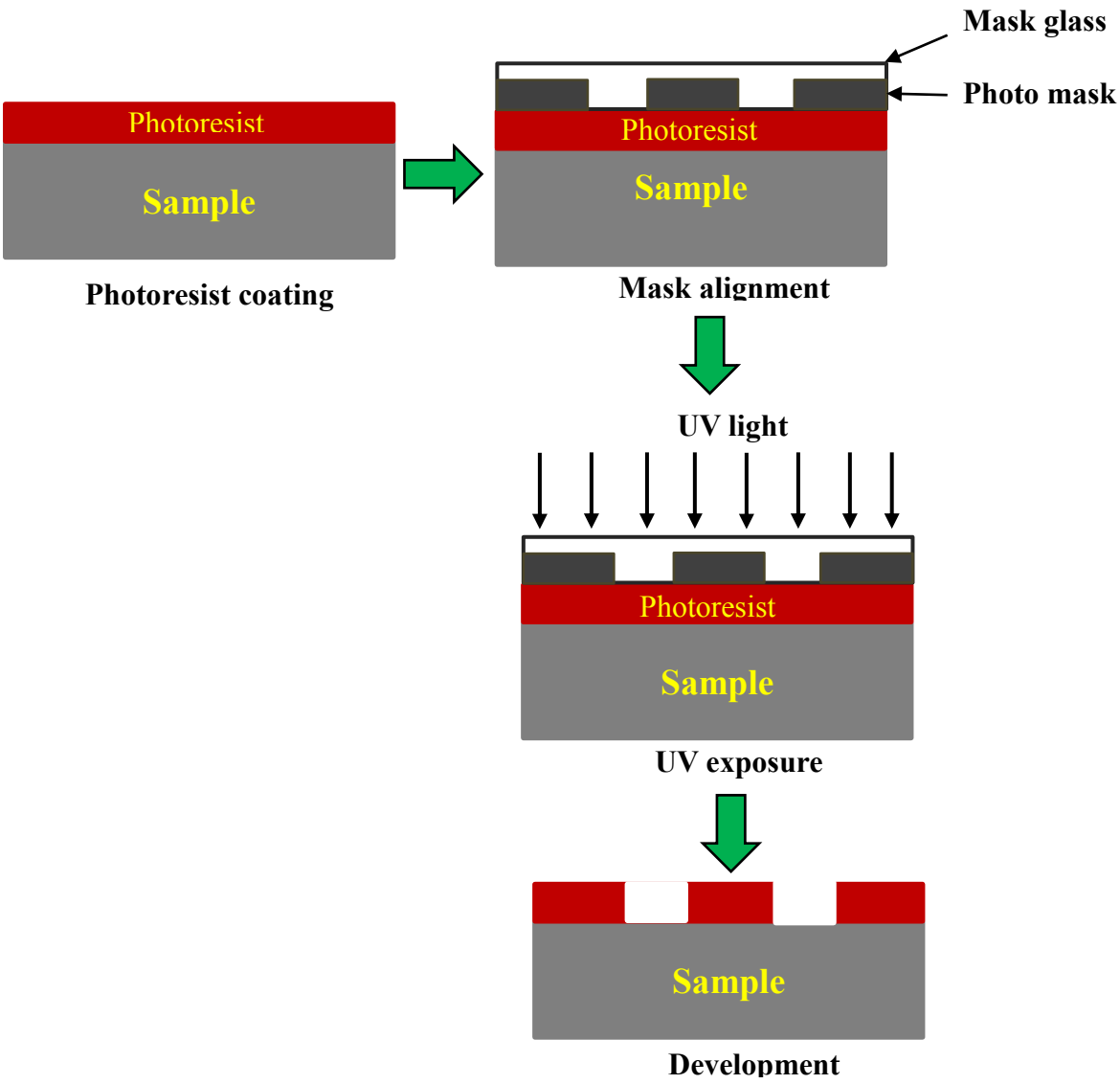

Fig. 3.2: Schematic of a single layer photolithography steps.

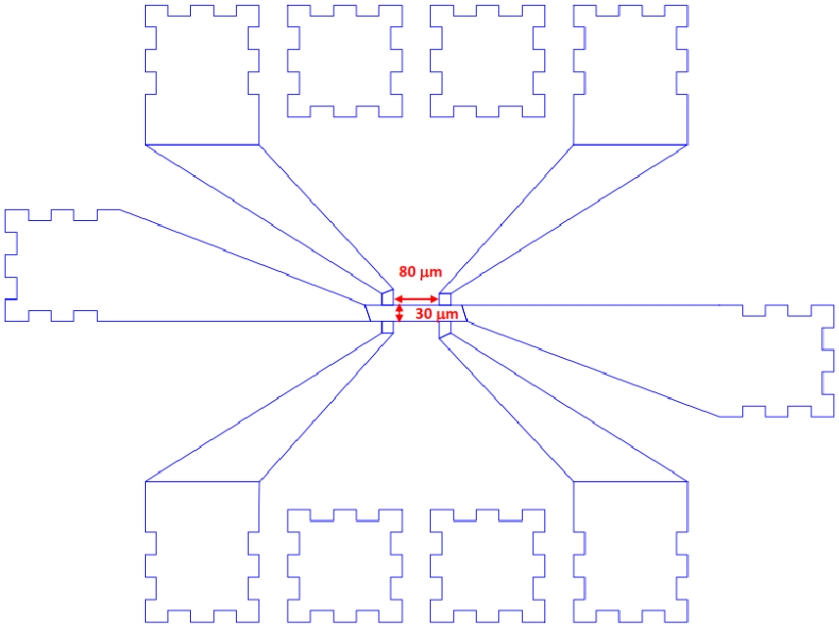

Fig. 3.3: Hall bar pattern (80 × 30 μm^2) in a photo mask with Ohmic contact six pads. Middle pads are used for top gate metal.

3.2.2 Mesa etching

Etching is used to remove material selectively in order to create electrical contacts or isolated individual devices. The parts of the material, which should remain, are protected by the photoresist while without photoresist parts are removed by *wet etching*. Wet etching has a high selectivity (the etch rate strongly depends on the material) and it does not damage the material. Etching solution contains strong oxidizer, such as H_2O_2 which oxides top surface of the semiconductor pattern and dissolving them by using acid such as HCl and H_2O [46].

The photolithography pattern of the sample (InSb/AlInSb hetrostructures) is immersed in a solution made up of 3% H_2O_2, 2.5% HF (hydrogen fluoride), and 85% lactic acid in the ratio 6:3:1, respectively at 10°C. After being rinsed by DIW for one minute, photoresist is then removed in acetone and washed followed by IPA, water and blown dry with N_2 gas jet. The height of etched step is measured immediately by profilometer (Dektak3ST). We etch 100 nm below the QWs to make the proper contact

with the InSb 2DEG. We measure the etch rate is found to be ~600A°/sec which is too fast. Hence, we dilute the etchant solution with 20 parts H_2O + 1 part etchant [3% H_2O_2, 2.5% HF (hydrogen fluoride), and 85% lactic acid in the ratio 6:3:1, respectively]. The diluted solution gives the rate of ~ 52 A°/sec and 56 A°/sec for our wafers t335 and t138, respectively.

3.2.3 Ohmic contacts

Metal contacts are needed to measure InSb 2DEG. The samples are cleaned and photolithography process follows until develop same as described in section 3.2.1. Indium metals are deposited as Ohmic contacts using electron-beam (e-beam) evaporation. The thickness of indium is measured by profilometer (Dektak3ST) and found to be ~ 4500 A°. The samples are then immersed in acetone (1 hour) and flushed over by acetone to remove photoresist, which is so-called lift-off process. Finally, samples are washed by DIW and blown dry with N_2 gas jet.

Table 3.1: Parameters of the InSb 2DEG confine in a 20 nm-wide InSb QW at 2 K.

Samples name	**Electron density n_s (m^{-2})**	**Mobility μ (m^2/Vs)**
t335	2.8×10^{15}	13.3
t138	2.7×10^{15}	5.3

3.3 Top gate fabrication using atomic layer deposition (ALD) technique

3.3.1 Mechanism of ALD technique

Atomic layer deposition (ALD), previously called atomic layer epitaxy (ALE) has been invented in 1974 by T. Suntola [47-49] for depositing polycrystalline and amorphous thin films for electroluminescent (EL) flat panel displays. The reactants are pulsed onto the substrates at a time in ALD process. Between the reactant pulses, excess reactants and reaction products are purged or evacuated by inert gas. This characteristic feature of ALD distinguishes it from closely related chemical vapour deposition (CVD) even similar chemical reaction that it breaks the CVD reaction into two half-reactions, keeping the precursor materials separate during the reaction. The experimental parameters, i.e., substrate temperature, reactant pressure and their exposure times, and the lengths of the purging periods, are adjusted in a way that all the surface reactions are saturative and purging steps are complete, removing all the other precursor molecules except those which have chemisorbed or undergone exchange reactions with the surface groups. Under such conditions, the film growth is self-limiting which ensures that it is stable with excellent uniformity and accurate thickness controlled simply by the number of reaction cycles repeated.

The continuing drive to shrink silicon devices will soon require the thickness of SiO_2 as the gate oxide in metal oxide semiconductor field effect transistors (MOSFET), the dominant device in today's integrated circuits, is projected to be scaled down to 1 nm, which is correspond to four or five atomic layers, SiO_2 no longer serves as an insulator because of the tunneling current that runs through it [50]. Therefore, alternative materials with a permittivity higher than that of SiO_2 (3.9) are needed to be able to use thicker gate dielectrics in achieving the required capacitances without tunneling leakage currents, and ALD is a rapidly gaining acceptance technique to deposit such kind of gate dielectric. Besides, enormous research has also been continuing to replace traditional Si or strained

Si using high mobility III-V compound semiconductors as conduction channel materials integrating high-k dielectrics. This dream remains due to lack of high-quality, thermodynamically stable gate dielectric insulators on III-V that can match device criteria similar to SiO_2 on Si.

Al_2O_3 is a technologically important material due to its excellent dielectric properties, good adhesion, thermal and chemical stability, that makes it a promising candidate to replace SiO_2 in microelectronic devices. ALD deposited Al_2O_3 is widely used as a high quality gate dielectric on quantum structures of III-V compound semiconductors (GaAs, InAs, InGaAs, GaSb, etc.) [51-54]. Trimethylaluminium (TMA) is used as a precursor for aluminium in most of the studies to deposit Al_2O_3 using ALD technique and water as an oxygen source [51-56]. However, water (H_2O) produces OH radicals, which acts as an impurity at the interface and degrades the quality of the film. Strong oxidized ozone (O_3) is a replacement of H_2O as an oxygen source which minimizes the formation of OH radicals and reduces Al-Al defects at the interface as well as [57, 58].

We have succeeded in depositing high quality Al_2O_3 on the InSb QWs using ALD system (Savannah S-100, Cambridge Nano Tech. Inc.) with TMA [Al $(CH_3)_3$] and H_2O for first 1 nm (10 cycles) and rest of the cycles TMA and O_3 as a metal and oxygen source, respectively. The feasibility of this recipe has been described in chapter 4. The reaction cycles of ALD- Al_2O_3 deposition is schematically shown in Fig. 3.4.

Step-1: In air, H_2O vapour adsorbed by the semiconductor surface and forms hydroxyl groups. Sample places in the ALD reactor and TMA is pulsed into the reaction chamber. TMA reacts with adsorbed hydroxyl group and produces methane (CH_4) as a reaction product.

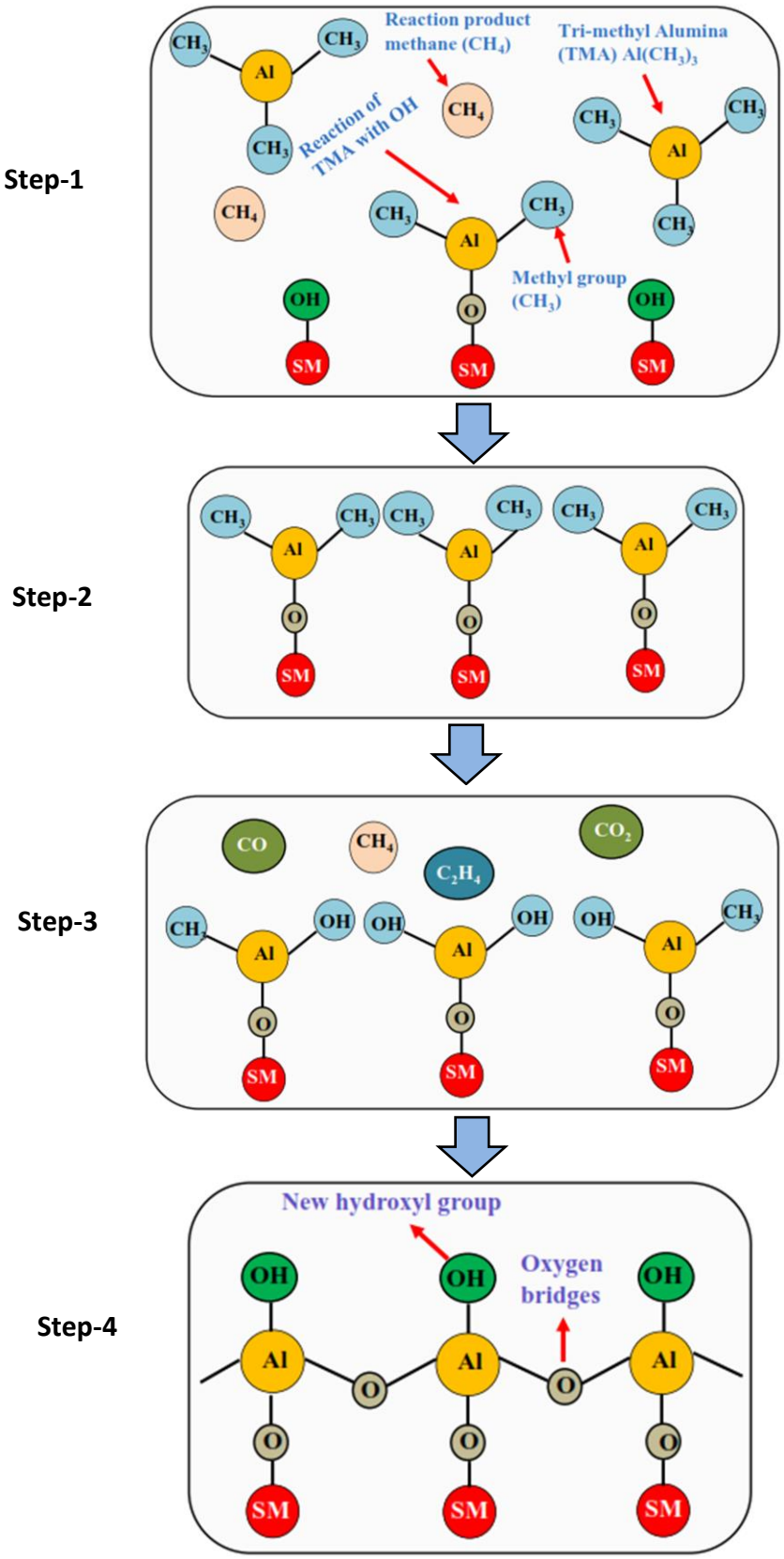

Fig. 3.4: Atomic layer deposition (ALD) cycles for depositing Al_2O_3 gate dielectric by using trimethylaluminium (TMA), water (H_2O) and ozone (O_3) as metal and oxygen sources, respectively.

Step-2: TMA reacts with hydroxyl groups until the surface is passivated. Note that, TMA doesn't react with itself, terminating the reaction to one layer. This causes the perfect uniformity of the ALD film. The excess TMA is purged with methane reaction products by nitrogen (N_2) inert gas.

Step-3: Ozone (O_3) is pulsed into the reaction chamber after purging the excess TMA and methane. O_3 reacts with the dangling metyl groups on the new surface forming aluminium-oxygen bridges and hydroxyl surface groups, waiting for new TMA pulse. The following reaction takes place:

$$2Al(CH_3)_3 + O_3 \longrightarrow Al_2O_3 + 3C_2H_6$$

and leads CO, CO_2, CH_4 and C_2H_4 as reaction products. Methane with others reaction products are pumped away.

Step-4: One TMA and one O_3 pulse forms one cycle. The thickness depends on the reaction cycle and growth temperature.

3.3.2 Sample preparation for top gate

Samples are cleaned in acetone (5 min), IPA (3 min), water (1 min) and followed by blown dry with N_2 gas jet. Samples are then covered by positive photoresist S1813G and UV exposes with top gate photomask by using photolithography process as described in section 3.2.1. After being cleaned by semico (1 min), water (1 min) and dry with N_2 gas jet, samples are then transferred to the ALD reactor. After the ALD process, samples are immersed in acetone (5 min) and sprayed with acetone to remove photoresist. Finally, samples are washed by water (1 min) and dry with N_2 gas jet.

3.4 Top gate metallization

Metal contacts are employed to connect top gate electrically. Samples are cleaned and spin coated by photoresist same as discussed in section 3.2.1. Indium is deposited as top gate metal using e-beam evaporation under the pressure of 2×10^{-4} Pa. A lift-off process is applied to remove photoresist. The thickness of indium is measured by profilometer about 450 nm.

3.5 Wire bonding

The Hall bars are separated from the sample chip using a Tempress-1713 manual scriber. The Hall bar is mounted on an 8-pin plastic leaded chip carrier (PLCC) with EPO-TEK H20E silver epoxy. An exceptional wire bonding with 45° feed is applied due to softness of the indium metal. A curing time of one hour at 120°C is employed to harden the epoxy. Top gated Hall bars are bonded by west bond 7476D manual wire bonder with high purity 25 μm gold wire. First bond with power 320 and time 40 *msec* is made to PLCC pad while second bond with power 450 and time 80 *msec* to complete the bonding cycle using calibration force 25 gm. Optical micrograph of a top gated Hall bar is shown in Fig. 3.5.

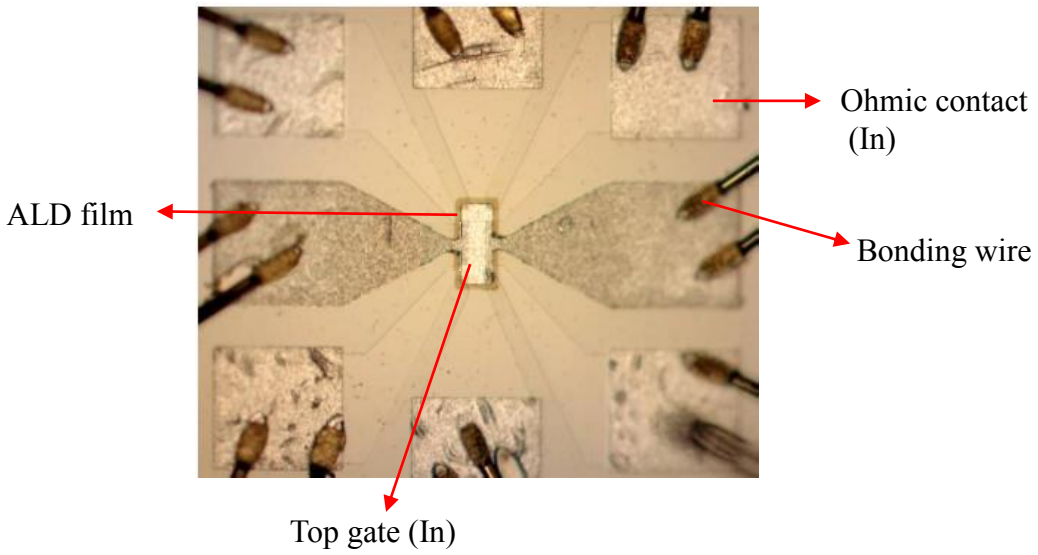

Fig. 3.5: Optical micrograph of a top gated InSb QW in Hall bar geometry with 8 contact pads.

3.6 Dilution refrigerator

The dilution refrigerator is a popular method of cooling in the milliKelvin (mK) temperature range using the two stable isotopes of helium: helium-3 (^{3}He) and helium-4 (^{4}He). The principle of the dilution refrigerator has been originally proposed by H. London in 1951 [59] and develops to its present form by H. London et al. [60] in 1962. When a mixture of the ^{3}He and ^{4}He is cooled below a critical temperature, it separates into two phases. The lighter "concentrated phase" is rich in ^{3}He and the heavier "dilute phase" (about 6.6% ^{3}He and 93.4% ^{4}He) is rich in ^{4}He. Due to enthalpy difference of the two phases, it is possible to cool down at mK region by evaporating the ^{3}He from the concentrated phase into the dilute phase.

A schematic diagram of a dilution refrigerator is shown in Fig. 3.6. The working principle of a dilution refrigerator is described in the following paragraphs:

- Some of the ^{4}He is siphoned off into the 1.5 K pot of the fridge. This causes some of the liquid helium in the pot to evaporate into gas. Thus lowering the temperature of the liquid. In this way, the temperature in the pot is lowered to 1.5 K.
- A precisely measured mixture of ^{3}He /^{4}He is passed via a pipe through the 1.5 K pot. As the liquid in the 1.5 K pot vaporizes, it draws heat away from the ^{3}He /^{4}He gas inside the pipe.
- The cooled gas condenses, dripping down into the still and mixing chamber below as a homogenous mixture of liquid.
- Conventional vacuum pumps lower the vapour pressure in the still, inducing evaporation and cooling the remaining liquid in the still down further. Vapour pressure of the ^{3}He is about 1000 times higher than that of the ^{4}He, therefore ^{3}He evaporates more rapidly than ^{4}He and it is mostly ^{3}He that evaporates off as a gas. While mostly ^{4}He is left behind in the still in liquid form. This begins the refrigeration cycle.

- The ^{3}He gas is funnelled into a condenser located within the 1.5 K pot, where it reliquefies, after passing through a gas handling systems comprises with liquid nitrogen (N_2) and liquid He cold traps for impurity (dirty gas) filtering.

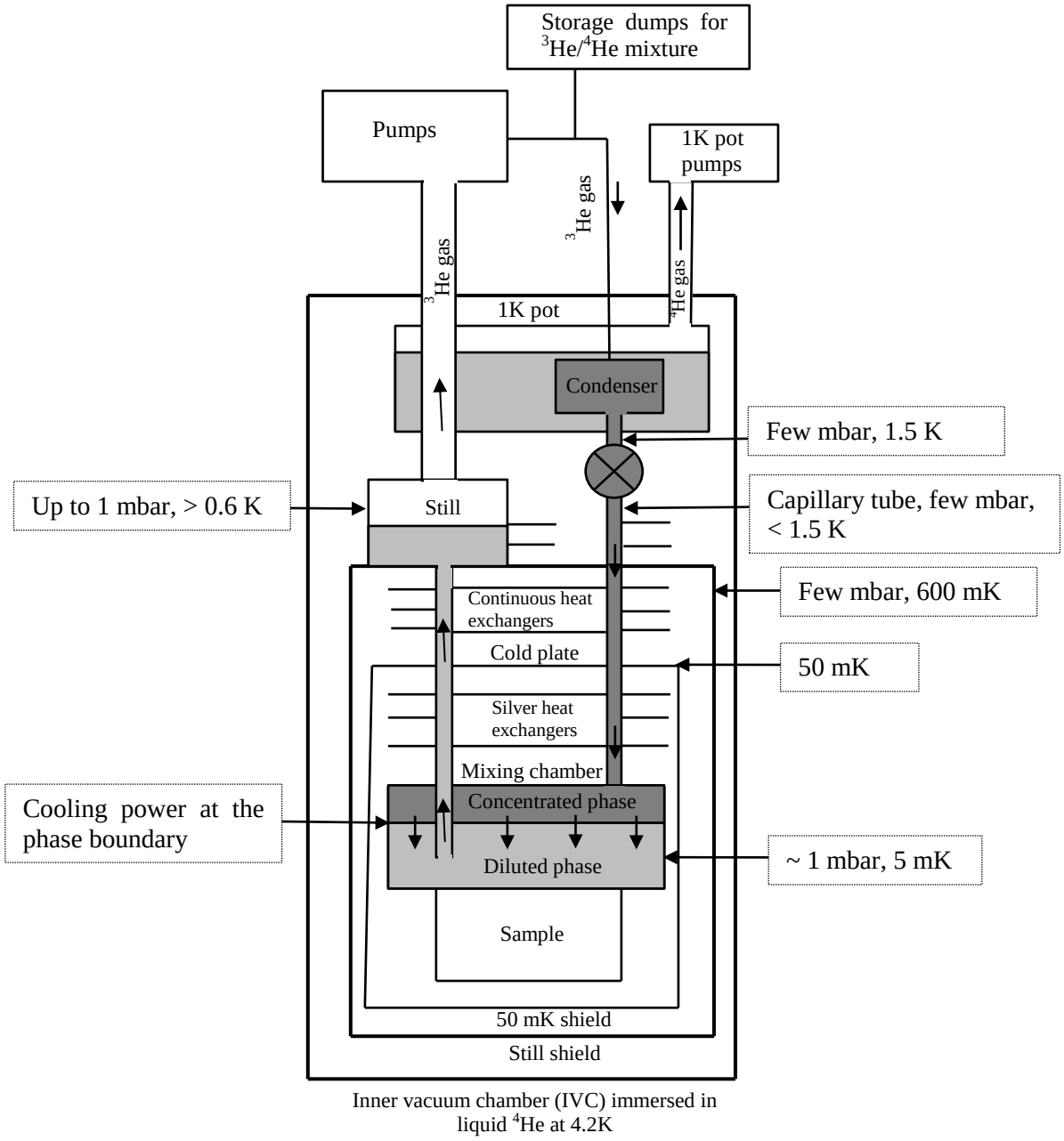

Fig. 3.6: Schematic diagram of a dilution refrigerator.

- A very narrow capillary tube located beneath the condenser provides the flow impedance that maintains the pressure required to make the helium liquefy. The ^{3}He passes through heat exchangers that cool it down further, to within a few mK of the target temperature.
- This mixing chamber is also connected to the still, so the ^{3}He liquid coming in from the condenser is being added to the mostly ^{4}He liquid that was funnelled into the chamber from the still at the beginning of the refrigeration cycle.

Phase separation is occurred below tri-critical temperature point at 0.86 K. The top layer in the mixing chamber contains mostly ^{3}He atoms. The heavier, bottom mixture contains mostly ^{4}He and some ^{3}He. Because ^{3}He atoms have been vaporizing out of the still, lowering the concentration of ^{3}He there, nature wants to restore the equilibrium concentration in the still where typically maintained temperature down to 0.6-0.7 K. Therefore, osmosis drives ^{3}He from the lower phase of the mixing chamber up to the still. This, in turn, disrupts the equilibrium in the lower phase. To restore that, ^{3}He atoms from the top layer must cross over to the bottom layer. In this way, we can continuously pull ^{3}He atoms from the top layer out of the bottom layer and have ^{3}He atoms from the top layer move across to the bottom to provide cooling.

^{3}He concentration and volume of the mixture are chosen correctly, so that the phase boundary is inside the mixing chamber and the liquid surface is in the still. The experimental apparatus is mounted in the mixing chamber or on the outside of the mixing chamber in vacuum and all the connections to the room temperature equipment is thermally anchored to reduce the heat load to the mixing chamber, giving the lowest possible base temperature.

3.7 Measurement system

Low temperature measurements are performed using AC and DC lock-in-techniques. In this technique, noise is minimized by measuring in a narrow frequency bandwidth. It is possible to measure the small signal even though signal is buried by noise sources many thousand times larger. We use four-probe configuration for measuring the voltage and different contacts those used to pass current through the sample. Transport measurement is done by applying a current 35 nA with 13.3 Hz lock-in frequency for both AC and DC.

Chapter 4

Characterization of InSb QWs with atomic layer deposited gate dielectrics

4.1 Introduction

Narrow bandgap semiconductor InSb has gained considerable interest recent years for next-generation high-speed electronics owing to its unique material properties including large dielectric constant (16.8), small effective mass (0.014 m_e, m_e is the free-electron mass), and high room-temperature mobility (77000 cm^2/Vs) [1-3, 14]. A two-dimensional electron gas (2DEG) formed in InSb quantum wells (QWs) has offered an advantage for spintronics device applications due to either strong spin-orbit coupling or a giant Landé *g*-factor [6, 8, 10, 22]. Implementation of electron-spin precession in a spin field-effect transistor (spin-FET) [15] and nuclear-spin coherence in a nanoscale region (e.g., quantum point contact) [16] entail a gated InSb QW.

Large conductance and high-density dislocation of an $Al_xIn_{1-x}Sb$ buffer layer between the QW and the substrate or low Schottky barrier heights [25] make InSb QWs challenging to fabricate back gate or Schottky contact. Considering these difficulties, we focus on top gate fabrication on the InSb QWs using atomic layer deposited (ALD) gate dielectrics Al_2O_3. We address another important issue for gate control InSb QWs that attracts less attention: the magnetoresistive (MR) property of the gated InSb QW strongly depends on layer structures of the QW, which has been elucidated by self-consistent Schrödinger-Poisson (SP) simulation and the two-carrier model. Characterization of gated InSb QWs with atomic layer deposited Al_2O_3 and optimum

QW layer structures for good gate controlled InSb QW have been discussed in this chapter.

4.2 Sample preparation

A cross section of the InSb QW (t335) with ALD-Al_2O_3 gate dielectric is shown in Fig. 4.1. The InSb/$Al_xIn_{1-x}Sb$ multilayers were grown on GaAs (001) substrates using an Intevac Modular Gen II molecular beam epitaxy system [44]. Two silicon (Si) δ-doped layers with the same donor density of 3.6×10^{15} m^{-2} (dashed line) are located above the QW: one is placed 15 nm above the QW to supply electrons in the well and the other 30 nm away from the top InSb layer to provide electrons to the surface state. Details of Hall bar fabrications are described in chapter 3. A Hall bar pattern (80×30 μm^2) is delineated by mesa etching and indium is employed as ohmic contacts using electron-beam deposition and lift-off to complete the fabrication process. After being washed with acetone, Isopropyl, and purified water and dried with nitrogen (N_2) gas jet, the InSb Hall bar is coated with a lift-off pattern of positive photoresist (S1813G) and get ready for gate dielectric deposition using ALD technique.

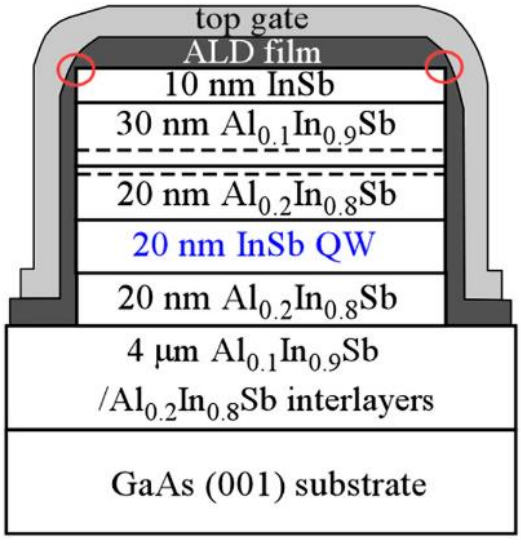

Fig. 4.1: Cross section of a gated InSb QW (t335) with ALD-Al_2O_3 dielectric. The dashed lines represent Si δ-doped layer and the area of ALD-Al_2O_3 at the corner of Hall bars is marked by a circle (red).

4.3 ALD recipe

The ALD technique has been extensively used to grow high-quality high-k dielectrics on quantum structures of III-V compound semiconductors (GaAs, InAs, GaN, GaSb, etc.) [24]. However, the study of the InSb QW with ALD gate dielectric is quite limited, possibly problem in interfacing high-k/(Al)InSb [25]. Surface treatment is applied in the work of Brask *et al.* [25] to remove native oxide and forms chalcogenide film as a bridge between ALD film and semiconductor materials. In contrast, we *directly* deposit Al_2O_3 on the top layer of the QWs using ALD technique.

The Al_2O_3 gate dielectric has grown using trimethylaluminum (TMA) with water (H_2O) and ozone (O_3) as the oxygen source using ALD system (Savannah S-100, Cambridge Nano Tech. Inc.). The growth rate depends on the reaction design, deposition temperature, purge time and the oxygen source, it may also depend on the substrate material. The Al_2O_3 film has been deposited by changing growth parameters and their results are listed in Table 4.1.

We deposit first ~1 nm using H_2O and TMA to prevent the photoresist pattern being damaged by O_3 in the latter process. The advantages of ozone as an alternative to H_2O have already been discussed in section 3.3.1. The photoresist hardens above the growth temperature 150°C as a consequence doesn't remove in the lift-off process. At low growth temperature (110°C), the gate dielectric shows a large leakage current. The growth temperatures 130 and 150°C ensure the successful lift-off of the photoresist (S1813G) and the gate dielectric shows a very small leakage current. Therefore, we select theme to deposit Al_2O_3 gate dielectric on the InSb QWs, even though deposition time is long (5~8 hours) due to the short purge time. The gated InSb QWs have been used in this chapter and chapter 6 with growth temperature 150°C and in chapter 5 with 130°C.

Table 4.1: Different ALD recipe for the deposition of Al_2O_3.

Deposition temperature (°C)	Growth rate (nm/cycle)	Purge time (sec)	Comment
110	0.1	TMA (60), H_2O (60), first ~1 nm TMA (50), O_3 (20), rest of the cycles	Large gate leakage current
130	0.104	TMA (30), O_3 (30)	Small gate leakage current Gate window (0.2 ~ -2.0V)
	0.118	TMA (30), H_2O (30)	Small gate leakage current Gate window (0.5 ~ -1.0V)
	0.097	TMA (50), H_2O (50), first ~1 nm TMA (40), O_3 (20), rest of the cycles	Small gate leakage current Gate window (1 ~ -4.0V)
150	0.111	TMA (20), H_2O (20), first ~1 nm TMA (20), O_3 (15), rest of the cycles	Small gate leakage current Gate window (0.7 ~ -5.0V)
170	0.115	TMA (8), H_2O (8), first ~1 nm TMA (15), O_3 (15), rest of the cycles	Photoresist becomes hard and doesn't remove
190	0.116	TMA (8), H_2O (8), first ~1 nm TMA (8), O_3 (10), rest of the cycles	Photoresist becomes hard and doesn't remove

4.4 Gate dielectric Al_2O_3 deposition

We have grown Al_2O_3 gate dielectric on the top InSb surface of the InSb QW at 150°C using TMA with H_2O and O_3 as the oxygen source. The first ten reaction cycles using alternate micropulses of H_2O (0.015s)/N_2 (waiting time: 20s) and TMA (0.015s)/N_2 (waiting time: 20s) are set to deposit ~ 1nm of Al_2O_3. An *in situ* surface treatment is then performed in 20 subsequent cycles using O_3 (0.025s)/N_2 pulses (waiting time: 15s).

Finally, 363 cycles using alternate micropulses of TMA (0.015s)/N_2 (waiting time: 20s) and O_3 (0.05s)/N_2 (waiting time: 15s) are taken under the pressure of 1 Torr. The thickness of the Al_2O_3 film is about 40 nm thick with a small root-mean-square roughness [61] of ~ 0.5 nm as seen by atomic force microscopy (inset of Fig. 4.2), indicating a smooth and dense surface. Indium is used as top-gate metal.

Gate leakage current density as a function of gate bias (V_g) is presented in Fig. 4.2. The current is measured between top-gate and Ohmic contact connected to the QW. Current leakage is clearly prominent at large negative V_g, suggesting high-quality of this dielectric. Note that, at positive bias, an electron channel is induced around the surface of a Hall bar covered by Al_2O_3 and is connected to the 2DEG via side wall contact. In this case, current leakage might occur even at a small bias provided the breakdown property of the thinner Al_2O_3 film across the Hall bar edge (circle mark in Fig. 4.1) deteriorates.

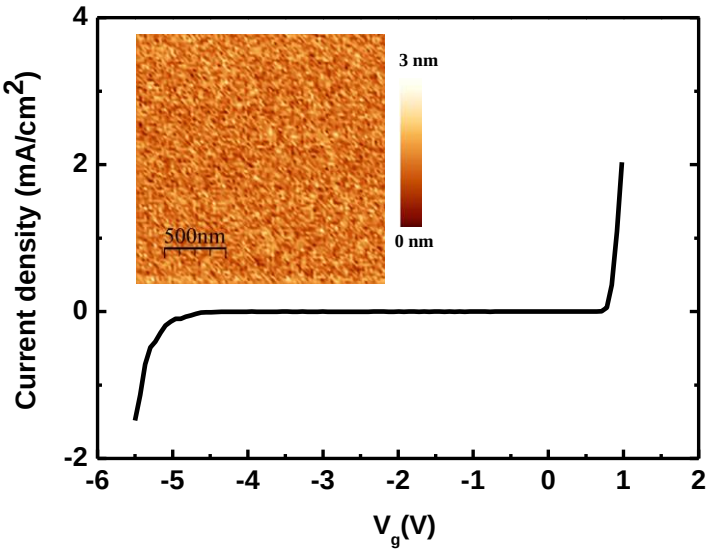

Fig. 4.2: Gate leakage current vs. gate voltage V_g at 2 K. Inset shows an AFM image of a 40 nm thick ALD-Al_2O_3 film grown at 150°C. The scale bar represents 500 nm.

4.5 Magnetotransport measurement

Magnetotransport measurements have been performed with AC current 35 nA and frequency 13.3 Hz at 2 K using standard lock-in technique. The longitudinal resistivity ρ_{xx} and Hall resistivity ρ_{xy} of the InSb QW vs. magnetic field (B) before the ALD process is depicted in Fig. 4.3. Standard clear single period oscillations are observed in ρ_{xx} and flat Hall plateau with equal quantized value in ρ_{xy} as shown in Fig. 4.3. Figure 4.4 shows the MR property of the gated InSb at different V_g. The MR property at V_g = 0 (green lines) exhibits an increasing resistivity background in ρ_{xx} and a sublinear field response in ρ_{xy}, which is very different from the standard MR property of single 2DEGs featured in Hall plateau with zero ρ_{xx} at high B [e.g., the cases of V_g = -1.6 V (blue lines) and the InSb QW before the ALD process as shown in Fig. 4.3]. This observation reminds us that a parallel conduction channel is formed in the sample after the ALD process.

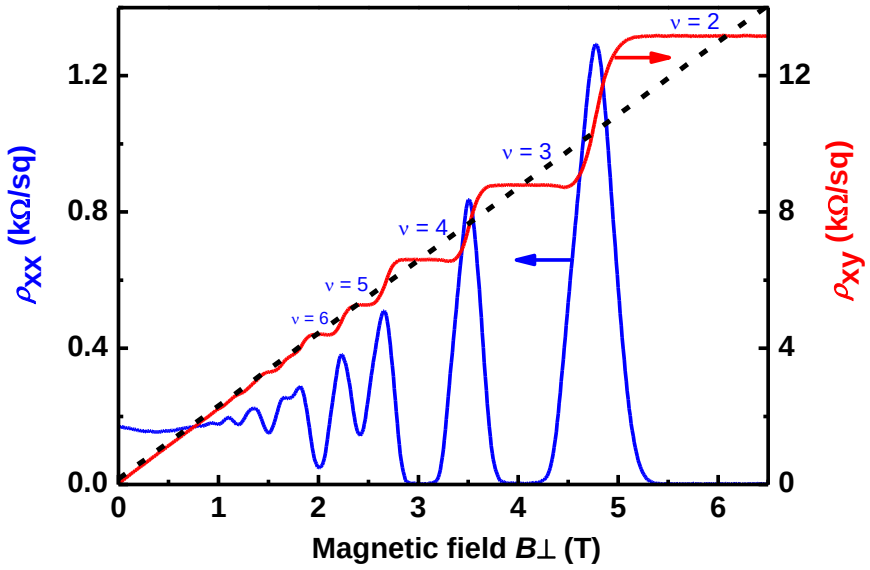

Fig. 4.3: Longitudinal resistivity ρ_{xx} and Hall resistivity ρ_{xy} as a function of magnetic-field (B) of the InSb QW before the ALD process with different filling factors (ν). The dashed line guides a linear dependence of ρ_{xy}-B.

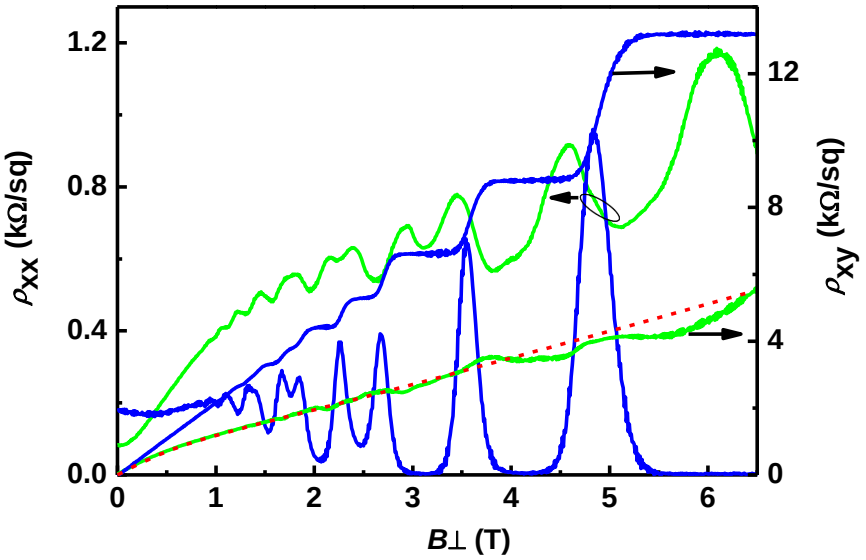

Fig. 4.4: Magnetic-field (B) dependent longitudinal resistivity ρ_{xx} and Hall resistivity ρ_{xy} of the InSb QW at V_g = 0 V (green lines) and V_g = -1.6V (blue lines). The dashed line is a fit for the nonlinear ρ_{xy}-B plot calculated by a two-carrier model.

4.6 Analysis of parallel conduction

Carrier density of parallel channel is calculated by a two carrier model (as described in section 2.7). According to a two-carrier model [43], the sublinear ρ_{xy}-B data fits well by $\rho_{xy} = \frac{\sigma_{xy}}{\sigma_{xx}^2 + \sigma_{xy}^2}$ (dashed line in Fig. 4.4), where $\sigma_{xx} = \frac{en_p\mu_p}{1+(\mu_p B)^2} + \frac{en_{QW}\mu_{QW}}{1+(\mu_{QW}B)^2}$, $\sigma_{xy} = \frac{en_p B\mu_p^2}{1+(\mu_p B)^2} + \frac{en_{QW}B\mu_{QW}^2}{1+(\mu_{QW}B)^2}$, and $n_{p(QW)}$ and $\mu_{p(QW)}$ are the density and mobility of electrons in the parallel channel (in the QW), respectively. The fit yields n_p = 3.64 × 10^{15} m^{-2}, μ_p = 0.53 m^2/Vs, and μ_{QW} = 17.5 m^2/Vs using the parameter value of n_{QW} = 3.86 × 10^{15} m^{-2} obtained from the fast Fourier transform (FFT) analysis of Shubnikov-de-Haas (SdH) oscillations in ρ_{xx} at V_g = 0 (green lines in Fig. 4.4). The parallel channel is found to be fully depleted by applying large negative V_g as reflected by the MR property of the single 2DEG [e.g., the case of V_g = -1.6 V (blue lines in Fig. 4.4)].

The gate bias-dependent n_{QW} and μ_{QW} are shown in Fig. 4.5. A large ratio of dn_{QW}/dV_g = 6.5 × 10^{14} $m^{-2}V^{-1}$ is determined (estimated in the range of -1.6V ≤ V_g ≤ 0.5V) and ensures the gate controllability of ALD-Al_2O_3 film on the InSb QWs. The 2DEG in

the QW is tuned by gate bias V_g over the bandgap of the top layer InSb, indicating that good interface between ALD-Al_2O_3 and InSb results the E_F is weakly pinned at the Al_2O_3/InSb interface.

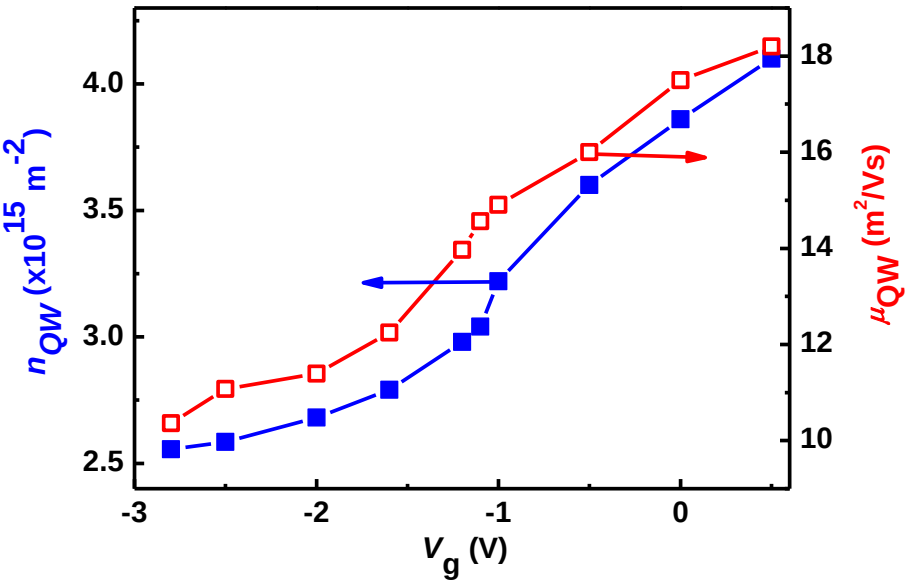

Fig. 4.5: Electron density (n_{QW}) and mobility (μ_{QW}) of the 2DEG confined in the InSb QW as a function of V_g. Note that the data at V_g > -1.2 V where a parallel conduction channel is formed in the sample are calculated from the FFT analysis of SdH oscillations in ρ_{xx} and the others from the classical Hall measurement.

The MR property is qualitatively understood by solving the SP equation self-consistently as discussed section 2.6. In this simulation, metal-insulator-semiconductor (MIS) contact is treated as a Schottky contact [62]. The CB edge profile of the InSb QW and electron density distribution ($|\Psi|^2$) in the QW calculated using the reported material parameters [63] are shown in Fig. 4.6, where E_F is at 0 eV and E_c at zero depth is equal to ϕ_B. The Schottky barrier height ϕ_B is determined by the property of the InSb surface and/or the Al_2O_3/InSb interface corresponds to the energy difference between the conduction band minimum (CBM) E_c of InSb and the E_F under thermal equilibrium conditions. The CB edge profile at $\phi_B \sim 0.128$ eV (black lines) is assigned to explain the MR property of the InSb QW before the ALD process as shown in Fig. 4.3.

Only the CB edge of the QW is below E_F, a single conduction channel (i.e., the 2DEG) exists in the sample. Note that ϕ_B is set to be larger than the mid-gap value (0.118 eV at 2 K) [41] of InSb based on the fact that the Fermi level is located above charge neutrality levels at the InSb surface [64], and hence the CB edge bends upwards after thermal equilibrium. As ϕ_B decreases after the ALD process (green line in Fig. 4.5), the CB discontinuity at the interface between the two $Al_xIn_{1-x}Sb$ layers (circle) lies below E_F and an additional electron channel emerges. This accounts for the parallel conduction channel formed in the InSb QW after the ALD process. The reduction of ϕ_B probably originates from the compensation of intrinsic acceptor surface states [64] and/or from the electric dipole effect [65, 66] at the Al_2O_3/InSb interface. The CB edge of the QW lowers due to reduction of the ϕ_B as shown in Fig. 4.6 (green line), resulting in an increase of n_{QW}. This is consistent with the experiment results showing that n_{QW} increases from 2.8 $\times 10^{15}$ m^{-2} to 3.86 $\times 10^{15}$ m^{-2} after the ALD process. A negative gate bias (V_g) increases ϕ_B,

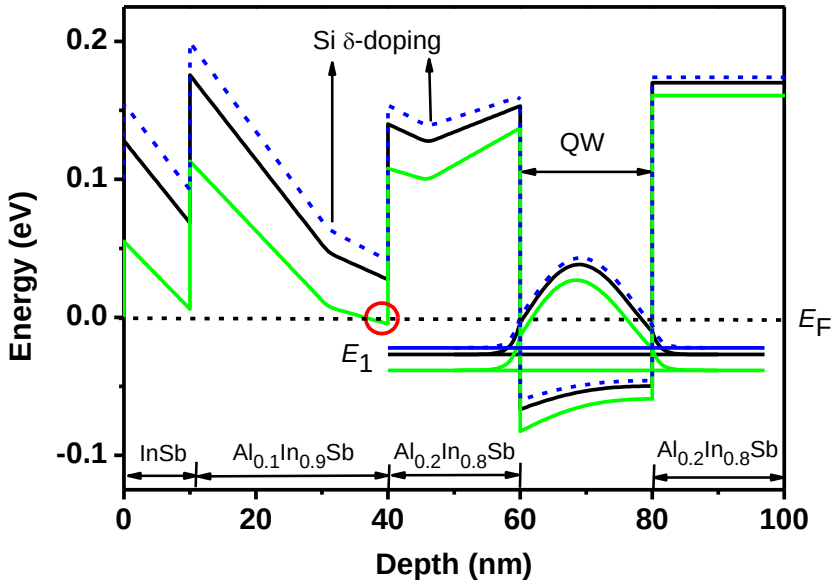

Fig. 4.6: Conduction-band profiles and the square of electron wave functions of the InSb QW obtained from self-consistent Schrödinger-Poisson solutions. The corresponding layer structures are indicated along the bottom axis. The band gap energy of all the layers is calculated at 2 K. The circle accentuates the CB discontinuity below the Fermi level E_F.

thereby the CB discontinuity raises entirely above the E_F as shown in Fig. 4.6 (blue dashed line). Therefore, the parallel channel is completely depleted and the standard MR property of single 2DEGs reappear (the case of V_g = -1.6 V, blue lines in Fig. 4.4). Since the CB edge of the QW moves to higher energy at negative V_g, n_{QW} decreases as shown in Fig. 4.5. At more negative V_g, n_{QW} becomes saturated because the valence band maximum (VBM) of InSb touches the E_F and holes accumulate at the surface to screen the gate potential to some degree [67]. Accordingly, the 2DEG in this sample is not completely depleted due to narrow bandgap surface layer (InSb) of the QW.

It is shown clearly that ϕ_B is modulated by V_g in a wide energy range, indicating that the Fermi level at the Al_2O_3/InSb interface is weakly pinned. Since the band gap of InSb in our sample is quite small, the E_F easily touches the CBM or VBM of these materials and thereby affects the MR property as described above. Because of this, it is expected that the InSb QW with a single layer of $Al_xIn_{1-x}Sb$ above the QW is more appropriate for gate control of the InSb 2DEG provided that the component x of $Al_xIn_{1-x}Sb$ is chosen properly by taking account of the band gap value (linear in x [42]) and the lattice mismatch to InSb. Indeed, Gilbertson *et al.* have employed the InSb QW with a single $Al_{0.15}In_{0.85}Sb$ layer above the QW for the study of gate control of the 2DEG but using sputtered SiO_2 as gate dielectric [10]. Such a QW structure together with the advantage of ALD in tailing the dielectric/semiconductor interface is believed to ensure complete depletion of the InSb 2DEG under gate control.

4.7 Conclusion

The MR property of a gated InSb QW with high-quality ALD-Al_2O_3 dielectric has been characterized at 2 K and discussed using the SP simulation and the two-carrier model. The magnetoresistance data demonstrate a parallel conduction channel in the sample at zero gate voltage (V_g). A good interface between Al_2O_3 and the top InSb layer ensures that the parallel channel is depleted at negative V_g and the density of two-dimensional electrons in the QW is tuned by V_g with a large ratio of 6.5×10^{14} $m^{-2}V^{-1}$ but saturates at

more negative V_g. Our results clearly demonstrate that both interface and QW layer structure issues are crucial for gate control of the InSb QW and also suggest that the QW layer structure with a higher bandgap surface layer is expected to be prevent hole accumulation at the surface by keeping the VB far from the E_F and thereby the 2DEG could be completely depleted as proposed by self-consistent Schrödinger-Poisson simulation.

Chapter 5

Gate depletion of an InSb two dimensional electron gas

Summary:

A split-gate technique is now widely used for the fabrication of semiconductor nanostructures (e.g., quantum point contacts and quantum dots): a negative bias on surface gates locally depletes the underlying two-dimensional electron gas (2DEG) confined to a quantum well (QW), leaving electrons only in a desired region surrounded by gated areas. This technique has already been applied to most semiconductors (Si, GaAs, InAs, InGaAs, etc.), but not to the typical narrow-gap semiconductor InSb even though InSb is particularly appealing for spintronics applications [8, 10, 22, 23, 34, 68-71].

We have grown a high quality Al_2O_3 gate dielectric on an InSb QW structure with an InSb QW surface layer using atomic layer deposition (ALD) (described in chapter 4). The Fermi level of this sample is tuned almost entirely across the band gap of InSb via gate bias. The good interface between the Al_2O_3 and InSb layers makes this possible, and allows us to study the importance of the layer sequence in gate controllability. However, the 2DEG in such a QW cannot be fully depleted because hole accumulation at the InSb surface layer screens the gate electric field. Based on a self-consistent Schrödinger-Poisson (SP) simulation, we predicted that the 2DEG would be depleted in an InSb QW with a wider-band-gap $Al_xIn_{1-x}Sb$ surface layer that is expected to prevent the hole accumulation as discussed in chapter 4.

In this chapter, we show experimental evidence that the 2DEG in an InSb QW with an $Al_{0.1}In_{0.9}Sb$ surface layer is completely depleted. Particularly noteworthy is that the $Al_{0.1}In_{0.9}Sb$ layer also has the advantages of suppressing a parallel conduction

channel and of keeping a relatively low interface trap density in the depletion process as revealed by our modified SP simulation. The success in gate depletion of the 2DEG enables the application of the split-gate technique to InSb QW structures, which has significant implications for realizing InSb-based spintronics.

Chapter 6

Measurement of nuclear-spin relaxation time T_1

Summary:

Nuclear-spin in semiconductor is a plausible candidate for future quantum computation due its long coherence time. Nuclear-spins quantum states manipulation by electrical/optical means using highly sensitive resistively detected nuclear magnetic resonance (RDNMR) has been based on the hyperfine interaction between nuclear and electron spins. Dynamic nuclear polarization (DNP) has been demonstrated in a single InSb two dimensional electron gas (2DEG) using RDNMR technique in tilted magnetic field [22, 23]. Pseudospin domain structure is account for a short and almost temperature independent nuclear-spin relaxation time T_1 in the quantum Hall ferromagnet (QHF). Information of nuclear-spins polarization as a function of filling factors and temperatures is necessary for further understanding of DNP mechanism as well as spin dynamic and implementation of nuclear-spin based quantum information processing (QIP). Gate controlled InSb QWs are required to study such kind of interesting topics, which have not been realized in the previous study [22, 23] due to lack of gate controllability. Successful gate deposition on InSb QWs allows us to study temperature dependent T_1 at different filling factors for the first time in the InSb 2DEG system using precise pump and probe technique. In this chapter we will present our results pump and probe experimental results and probable explanations.

We have successfully performed pump and probe experiment in a gate controlled InSb QW. Low energy collective spin texture excitations in the domain walls is account for short and almost temperature independence of T_1 in the QHF. On the other hand, T_1

becomes relatively long and strong temperature dependence with following Korringa law at around filling factor $\nu = 3$ which has been characterized by the absence of domain formation as well as collective spin texture. The RDNMR demonstration at elevated temperature in the QHF provides fundamental outlooks on the DNP and the dynamic of domain in the 2D ferromagnet. Our result clearly demands that InSb 2DEG is a plausible candidate for implementation of the high temperature nuclear-spin based quantum information processing due to its large Zeeman, cyclotron, and exchange energy.

Chapter 7

Concluding remarks

7.1 Summary

The renewed research effort has been paid more than four decades to replace main stream Si in advanced ultra-large-scale-integration (ULSI) digital applications or complementary metal-oxide-semiconductor (CMOS) technology by using III-V compound semiconductor material as a conduction channel due to its high mobility. The dearth of high quality gate dielectric insulators on III-V that can match device criteria similar to SiO_2 on Si, remains a dream to realizing a III-V metal-oxide-semiconductor field-effect-transistor (MOSFET) technology with commercial value. The typical semiconductor InSb has gained attention in high-speed electronics, future nuclear-spin-based quantum bits (qubits) operation and spintronics applications because of high room temperature mobility (77000 cm^2/Vs) and large spin-orbit coupling. The study of the InSb QW with gate is quite inadequate probably due to problem in interfacing between the gate insulator and top surface semiconductor. However, gate controlled InSb QWs is required to understand dynamic nuclear polarization (DNP) as well as its interaction with electron-spins and also coherent control of nuclear-spins in a nanoscale region (e.g., quantum point contact (QPC)) [16] for further implementation of nuclear-spins in qubits operation and electron-spins in a spin-FET [15]. Therefore, the present thesis has been concerned to fabricate good top gated InSb QW and its application to study the DNP by using highly sensitive resistively detected nuclear magnetic resonance (RDNMR) technique.

We have successfully fabricated high quality gate controlled InSb QW with InSb surface layer using atomic layer deposition (ALD) technique. The density of two-dimensional electron gas (2DEG) in the QW is tuned by gate bias (V_g) with a large ratio of 6.5×10^{14} $m^{-2}V^{-1}$, however, shows a parallel conduction at zero V_g. The parallel channel is depleted at negative V_g thanks to good interface between Al_2O_3 and the top layer InSb of the QW, but saturates at large negative V_g due to the Fermi level E_F touches the valence band (VB), thereby the hole accumulation at the InSb surface that screens the gate electric field. Accordingly, the 2DEG is not depleted in this sample. We propose that the 2DEG can be depleted in the InSb QW with higher band gap $Al_xIn_{1-x}Sb$ surface layer that is expected to prevent the hole accumulation at the interface and the electron accumulation at the discontinuity of multi layers band mismatch as suggested by the Self-consistent Schrödinger-Poisson (SP) simulation.

To investigate our proposal, we fabricate ALD-Al_2O_3 InSb QWs with higher band gap ($Al_{0.1}In_{0.9}Sb$) surface layer. The 2DEG in the InSb QW is completely depleted by application of a very small V_g (~ 0.9V) and the parallel conduction channel is strongly suppressed at zero V_g. The $Al_{0.1}In_{0.9}Sb$ surface layer is formed an excellent interface with Al_2O_3 that is reflected in the response of 2DEG density to V_g with a linear, sharp, and hysteresis free. Moreover, the interface traps density between $Al_{0.1}In_{0.9}Sb$ and Al_2O_3 is found to be lower than that of Al_2O_3/InSb, resulting a very weak E_F pinning as analysed by the SP simulation and an equivalent capacitance model. Therefore, the 2DEG density is tuned by a very small V_g. This realization paves the way to fabricate split-gate defined InSb nanodevices (e.g., QPC).

Finally, we have demonstrated temperature dependent nuclear-spin relaxation time T_1 at different filling factors by using pump and probe technique in a gated InSb QW. Low energy collective spin texture excitations in the domain walls between two adjacent domains is account for short and almost temperature independence of T_1 in the quantum Hall ferromagnet (QHF). On the other hand, relatively long and temperature

dependence of T_1 with following Korringa law around filling factor $\nu = 3$ have been elucidated by the absence of domain formation as well as collective spin texture. We also observe the RDNMR signal at elevated temperature up to 6 K in the QHF that provides fundamental outlooks on the DNP and makes the InSb 2DEG a credible candidate for implementation of high temperature nuclear-spin based quantum information processing.

7.2 Future works

Gate controlled InSb QWs are now available with completely depleted 2DEG. Fabrication of split-gate-defined InSb QPC is now in progress. Quantized conductance and coherent control of nine quadrupole splittings of ^{115}In could be investigated. Several issue deserves a close look, even though, our results are very interesting. We could not use completely depleted 2DEG sample because of low mobility. We perform the RDNMR using high mobility sample with InSb surface layer that limits our study region between ν=2 and 3 due to saturation of the 2DEG in the QW at large negative V_g. Therefore, a high mobility InSb QW with higher band gap top surface layer is expected to be extended the RDNMR study region and provides further understanding of the nuclear-spin relaxation phenomena.

Bibliography

[1] S. Datta, T. Ashley, J. Brask, L. Buckle, M. Doczy, M. Emeny, D. Hayes, K. Hilton, R. Jefferies, T. Martin, T. J. Phillips, D. Wallis, P. Wilding, and R. Chau, IEDM-Tech. Dig. 763 (2005).

[2] R. Chau, S. Datta, M. Doczy, B. Doyle, B. Jin, J. Kavalieros, A. Majumdar, M. Metz, and M. Radosavljevic, IEEE Trans. Nanotech. 4, 153 (2005).

[3] T. Ashley, L. Buckle, S. Datta, M. T. Emeny, D. G. Hayes, K. P. Hilton, R. Jefferies, T. Martin, T. J. Philips, D. J. Wallis, P. J. Wilding, and R. Chau, Electron. Lett. 43, 777 (2007).

[4] http://www.ioffe.ru/SVA/NSM/Semicond/InSb/bandstr.html#Basic,Ioffe Institute, The Russian Academy of Sciences, Russia (2013).

[5] S. M. Sze and K. K. Ng, Physics of Semiconductor Device, 3rd edition (Wiley & Sons, New York) (2007).

[6] R. L. Kallaher, J. J. Heremans, N. Goel, S. J. Chung, and M. B. Santos, Phys. Rev. B 81, 075303 (2010).

[7] J. B. Miller, D. M. Zumbühl, C. M. Marcus, Y. B. Lyanda-Geller, D. Goldhaber-Gordon, K. Campman, and A. C. Gossard, Phys. Rev. Lett., 70, 076807 (2003).

[8] K. F. Yang, H. W. Liu, T. D. Mishima, M. B. Santos, K. Nagase, and Y. Hirayama, New J. Phys. 13, 083010 (2011).

[9] V. Umansky, M. Heiblum, Y. Levinson, J. Smet, J. Nubler, M. Dolev, J. Crystal Growth 311, 1658 (2009).

[10] A. M. Gilbertson, W. R. Branford, M. Fearn, L. Buckle, P. D. Buckle, T. Ashley, and L. F. Cohen, Phys. Rev. B 79, 235333 (2009).

[11] S. A. Solin, D. R. Hines, J. S. Tsai, Y. A. Pashkin, S. J. Chung, N. Goel, and M. B. Santos, IEEE Trans. Magn. 38, 89 (2002).

[12] S. A. Solin, D. R. Hines, A. C. H. Rowe, J. S. Tsai, Y. A. Pashkin, S. J. Chung, N. Goel, and M. B. Santos, Appl. Phys. Lett. 80, 4012 (2002).

[13] A. M. Gilbertson, A. Kormanyos, P. D. Buckle, M. Fearn, T. Ashley, C. J. Lambert, S. A. Solin, and L. F. Cohen, Appl. Phys. Lett. 99, 242101 (2011).

[14] T. D. Mishima, M. Edirisooriya, and M. B. Santos, Appl. Phys. Lett. 91, 062106 (2007).

[15] S. Datta and B. Das, Appl. Phys. Lett. 56, 665 (1990).

[16] G. Yusa, K. Muraki, T. Takashina, K. Hashimoto, and Y. Hirayama, Nature 434, 1001 (2005).

[17] K. Hashimoto, K. Muraki, T. Saku and Y. Hirayama, Phys. Rev. Lett., 88, 176601 (2002).

[18] M. Dobers and K. v. Klitzing J. Schneider G. Weimann K. Ploog, Phys. Rev. Lett. 61, 1650 (1988).

[19] O. Stern, N. Freytag, A. Fay, W. Dietsche, J. H. Smet, K. von Klitzing, D. Schuh, and W. Wegscheider, Phys. Rev. B 70, 075318 (2004).

[20] Y. Hirayama, G. Yusa, K. Hashimoto, N. Kumada, T. Ota, and K. Muraki, Semicond. Sci. Technol. 24, 023001 (2009) [Topical Review].

[21] Y. Hirayama, Contact Hyperfine Interactions in Semiconductor Heterostructures, in Comprehensive Semiconductor Science and Technology (vol. 2), edited by P. Bhattacharya, R. Fornari, and H. Kamimura (Elsevier Amsterdam, 2011).

[22] H. W. Liu, K. F. Yang, T. D. Mishima, M. B. Santos, and Y. Hirayama, Phys. Rev. B 82, 241304(R) (2010).

[23] K. F. Yang, H. W. Liu, K. Nagase, T. D. Mishima, M. B. Santos, and Y. Hirayama, Appl. Phys. Lett. 98, 142109 (2011).

[24] S. Oktyabrsky and P. D. Ye, *Fundamentals of III-V Semiconductor MOSFETs* (Springer, New York, 2010).

[25] J. K. Brask, S. Datta, M. L. Doczy, J. M. Blackwell, M. V. Metz, J. T. Kavalieros, and R. S. Chau, U.S. Patent No. 7,485,503 (2009).

[26] G. A. Bastard, Wave Mechanics Applied to Semiconductor Heterostructures, Les Editions de Physique, Paris, 1988.

[27] J. A. Chu and A. Sher, Device Physics of Narrow Gap Semiconductors, (Springer, Ney York) (2010).

[28] T. Ando, A. B. Fowler and F. Stern, Rev. Mod. Phys. 54, 437 (1983).

[29] R. B. Lauhlin, Phys. Rev. B 23, 5632 (1981).

[30] K. v. Klitzing, G. Dorda and M. Pepper, Phys. Rev. Lett. 45, 494 (1980).

[31] R. E. Prange and S. M. Girvin, The Quantum Hall Effect, (Springer-Verlag, New York) (1987).

[32] A. Berg, M. Dobers, R. R. Gerhardts and K. v. Klitzing, Phys. Rev. Lett., 64, 2563 (1990).

[33] I. D. Vagner and T. Maniv, Phys. Rev. Lett., 61, 1400 (1988).

[34] I. Žutic, J. Fabian, and S. Das Sarma, Rev. Mod. Phys. 76, 323 (2004).

[35] R. J. Nicholas, R. J. Haug, K. von Klitzing, and G. Weimann, Phys. Rev. B 37, 1294 (1988).

[36] T. Jungwirth and A. H. MacDonald, Phys. Rev. B 63, 035305 (2000).

[37] E. P. De Poortere, E. Tutuc, S. J. Papadakis, and M. Shayegan, Science 290, 1546 (2000).

[38] T. Jungwirth and A. H. MacDonald, Phys. Rev. Lett. 87, 216801 (2001).

[39] K. Muraki, T. Saku, and Y. Hirayama, Phys. Rev. Lett. 87, 196801 (2001).

[40] I-H Tan, G. L. Snider, D. L. Chang and E. L. Hu, J. Appl. Phys. 68, 4071 (1990).

[41] I. Vurgaftman, J. R. Meyer, and L. R. Ram-Mohan, J. Appl. Phys. 89, 5815 (2001).

[42] N. Dai, F. Brown, P. Barsic, G. A. Khodaparast, R. E. Doezema, M. B. Johnson, S. J. Chung, K. J. Goldmmer, and M. B. Santos, Appl. Phys. Lett. 73, 1101 (1998).

[43] M. J. Kane, N. Apsley, D. A. Anderson, L. L. Taylor, and T. Kerr, J. Phys. C: Solid State Physics 18, 5629 (1985).

[44] M. Edirisooriya, T. D. Mishima, and M. B. Santos, J. Vac. Sci. Technol. 25, 1063 (2007).

[45] T. D. Mishima, M. Edirisooriya, and M. B. Santos, Appl. Phys. Lett. 91, 062106 (2007).

[46] G. C. Desalvo, Ron Kaspi, and C. A. Bozada, J. Electrochem. Soc. 141, 3526 (1994).

[47] T. Suntola, J. Antson, US Patent no. 4,058,430, (1977).

[48] M. Leskelä, M. Ritala, Thin Solid Films 409,138 (2002).

[49] M. Ritala, K. Kukli, M. Leskela, A. Rahtu,T. Sajavaara, P. I. Raisanen, and J. Keinonen, Science 288, 319 (2000).

[50] D. A. Muller, T. Sorsch, S. Moccio, F. H. Baumann, K. Evans-Lutterodt & G. Timp, Nature 399, 758 (1999).

[51] P. D. Ye, G. D. Wilk, B. Yang, J. Kwo, S. N. G. Chu, S. Nakahara, H.-J. L. Gossmann, J. P. Mannaerts, M. Hong, K. K. Ng, and J. Bude, Appl. Phys. Lett. 83 180 (2003).

[52] J. Wu, E. Lind, R. Timm, Martin Hjort, A. Mikkelsen, and L. –E. Wernersson, Appl. Phys. Lett. 100 132905 (2012).

[53] Y. Xuan, Y. Q. Wu, T. Shen, T. Yang, P. D. Ye, IEEE Int. Electron Dev. Meet Technol Dig, 637 (2007).

[54] A. Ali, H. S. Madan,A. P. Kirk,D. A. Zhao,D. A. Mourey,M. K. Hudait,R. M. Wallace,T. N. Jackson, B. R. Bennett, J. B. Boos,and S. Datta, Appl. Phys. Lett. 97, 143502 (2010).

[55] Y. Kim, S. M. Lee, C. S. Park, S. I. Lee, and M. Y. Lee, Appl. Phys. Lett. 71, 3604 (1997).

[56] R. Matero, A. Rahtu, M. Ritala, M. Leskela, and T. Sajavaara, Thin Solid Films 368, 1 (2000).

[57] J. B. Kim, D. R. Kwon, K. Chakrabarti, Chongmu Lee, K. Y. Oh, and J. H. Lee, J. Appl. Phys. 92, 6739 (2002).

[58] D. N. Goldstein, J. A. McCormick, and S. M. George, J. Phys. Chem. C 112, 19530 (2008).

[59] H. London, Proceedings of the International Conference on Low Temperature Physics, (Oxford Univ. Press, Oxford, 1951).

[60] H. London, G. R. Clarke, and E. Mendoza, Phys. Rev. 128, 1992 (1962).

[61] I. Horcas, R. Fernandez, J. M. Gomez-Rodriguez, J. Colchero, J. Gomez Herrero, and A. M. Baro, Rev. Sci. Instrum. 78, 013705 (2007).

[62] S. Birner, Ph. D. thesis, Technical University of Munich, Germany, (2011).

[63] J. M. S. Orr, P. D. Buckkle, M. Fearn, P. J. Wilding, C. J. Bartlett, M. T. Emeny, L. Buckle, and T. Asshley, Semicond. Sci. Technol. 21, 1408 (2006).

[64] P. D. C. King, T. D. Veal, M. J. Lowe, and C. F. McConville, J. Appl. Phys. 104, 083709 (2008).

[65] R. T. Tung, Phys. Rev. B 64, 205310 (2001).

[66] J. Hu, K. C. Saraswat, and H. S. Philip Wong, Appl. Phys. Lett. 99, 092107 (2011).

[67] For the sample of this work (sample 1), we have only measured the SdH oscillations of ρ_{xx} up to V_g = -2.8 V. At V_g = -2.8 V, ρ_{xx} is zero at filling factors of one and two, indicating a single 2DEG feature without parallel channels. More recently, we have measured the SdH oscillations of ρ_{xx} up to -5 V in another sample fabricated from the same wafer and the same ALD process as sample 1. It is found that ρ_{xx} at filling factors of one and two increases as V_g increases from -4.5 V. This clearly suggests that an addition parallel channel appears, which is assigned to the hole accumulation as indicated in the SP simulation. However, the density and mobility of hole carriers are too low to be estimated from the two-carrier model.

[68] G. A. Khodaparast, R. C. Meyer, X. H. Zhang, T. Kasturiarachchi, R. E. Doezema, S. J. Chung, N. Goel, M. B. Santos, Y. J. Wang, Physica E 20, 386 (2004).

[69] C. M. Jaworski, R. C. Myers, E. Johnston-Halperin, and J. P. Heremans, Nature 487, 210 (2012).

[70] S. Nadj-Perge, V. S. Pribiag, J. W. G. van den Berg, K. Zou, S. R. Plissard, E. P. A. M. Bakkers, S. M. Frolov, and L. P. Kouwenhoven, Phys. Rev. Lett. 108, 166801 (2012).

[71] H. A. Nilsson, P. Caroff, C. Thelander, M. Larsson, J. B. Wagner, L. Erik Wernersson, L. Samuelson, and H. Q. Xu, Nano Lett. 9, 3151 (2009); M. T. Meng, C. L. Yu, G. Y. Huang, M. Larsson, P. Caroff, and H. Q. Xu, Nano Lett. 12, 6414 (2012).

[72] J. W. G. van den Berg, S. Nadj-Perge, V. S. Pribiag, S. R. Plissard, E. P. A. M. Bakkers, S. M. Frolov, and L. P. Kouwenhoven, Phys. Rev. Lett. 110, 066806 (2013).

[73] V. S. Pribiag, S. Nadj-Perge, S. M. Frolov, J. W. G. van den Berg, I. van Weperen, S. R. Plissard, E. P. A. M. Bakkers and L. P. Kouwenhoven, Nature Nanotechnology 8,170 (2013).

[74] C. H. Hou, M. C. Chen, C. H. Chang, T. B. Wu, C. D. Chiang, and J. J. Luo, J. Electrochemical Society, 155 (9), G180 (2008).

[75] S. Luryi, Appl. Phys. Lett. 52, 501 (1988).

[76] K. Suzuki, Y. Harada, F. Maeda, K. Onomitsu, T. Yamaguchi, and K. Muraki, Appl. Phys. Express 4, 125702 (2011).

[77] J. Hinz, H. Buhmann, M. Schäfer, C. R. Becker, and L. W. Molenkamp, Semicond. Sci. Technol. 21, 501 (2006).

[78] S. Nakata, K. Saito, and M. Shimada, Appl. Phys. Lett. 87, 223110 (2005).

[79] M. Choi, A. Janotti, and C. G. Van de Walle, J. Appl. Phys. 113, 044501 (2013).

[80] G. F. Giuliani and J. J. Quinn, Phys. Rev. B 31, 6228 (1985).

[81] S. Koch, R. J. Haug, and K. v. Klitzing, M. Razeghi, Phys. Rev. B 47, 4048 (1993).

[82] W. Desrat, D. K. Maude, M. Potemski, J. C. Portal, Z. R. Wasilewski, and G. Hill, Phys. Rev. Lett. 88, 256807 (2002).

[83] X. C. Zhang, G. D. Scott, and H. W. Jiang, Phys. Rev. Lett. 98, 246802 (2007).

[84] A. W. Overhauser, Phys. Rev. 89, 689 (1953).

[85] G. Gervais, H. L. Stormer, D. C. Tsui, P. L. Kuhns, W. G. Moulton, A. P. Reyes, L. N. Pfeiffer, K. W. Baldwin, and K. W. West, Phys. Rev. Lett. 94, 196803 (2005).

[86] L. A. Tracy, J. P. Eisenstein, L. N. Pfeiffer, and K. W. West, Phys. Rev. B 73, 121306R (2006).

[87] C. R. Bowers, G. M. Gusev, J. Jaroszynski, J. L. Reno, and J. A. Simmons, Phys. Rev. B 81, 073301 (2010).

[88] C. R. Dean, B. A. Piot, G. Gervais, L. N. Pfeiffer, and K. W. West, Phys. Rev. B 80, 153301 (2009).

[89] G. P. Guo, X. J. Hao, T. Tu, Y. J. Zhao, Z. R. Lin, G. Gao, H. O. Li, C. Zhou, G. C. Guo, and H. W. Jiang, Phys. Rev. B 81, 041306(R) (2010).

[90] X. G. Wu and S. L. Sondhi, Phys. Rev. B 51, 14 725 (1995).

[91] D.K. Maude, S. Marty, L.B. Rigal, M. Potemski, J.C. Portal, Zb. Wasilewski, M. Henini, L. Eaves, G. Hill, M.A. Pate, Physica (Amsterdam) 249-251B, 1 (1998).

[92] N. Kumada, K. Muraki, and Y. Hirayama, Science 313, 329 (2006).

[93] J. Korringa, Physica 16, 601 (1950).

[94] H. Takahashi, M. Kawamura, S. Masubuchi, K. Hamaya, T. Machida, Y. Hashimoto, and S. Katsumoto, Appl. Phys. Lett. 91, 092120 (2007).

[95] R. Waser, Nanoelectronics and Information Technology (Berlin: Wiley-VCH) (2003).

[96] E. Joe Brewer and M. Gill, Nonvolatile Memory Technologies with Emphasis on Flash (Hoboken, NJ: Wiley) (2008).

[97] D. Khang and S. M. Sze, Bell Syst. Tech. J., 46, 1288 (1967).

[98] J. R. Cricchi, F. C.Blaha, and M.D. Fitzpatrick, IEEE IEDM Tech. Dig., p.126, (1973).

[99] Y. Yatsuda, T. Hagiwara, S. Minami, R. Kondo, K. Uchida, and K. Uchiumi, Jpn. J. Appl. Phys. 21, 85 (1982).

[100] S. Iida and K. Ito, J. Electrochem. Soc., 118, 768 (1971).

List of Publications and Presentations

Publications:

1. M. M. Uddin, H. W. Liu, K. F. Yang, K. Nagase, T. D. Mishima, M. B. Santos, and Y. Hirayama, "Characterization of InSb quantum wells with atomic layer deposited gate dielectrics" *Appl. Phys. Lett.* **101**, 233503 (2012).

2. M. M. Uddin, H. W. Liu, K. F. Yang, K. Nagase, T. D. Mishima, M. B. Santos, and Y. Hirayama, "Gate depletion of an InSb two dimensional electron gas" Under review (*Appl. Phys. Lett.*).

Presentations:

1. M. M. Uddin, K. F. Yang, H. W. Liu, K. Nagase, T. D. Mishima, M. B. Santos, and Y. Hirayama, "Collective nature of quantum Hall ferromagnets revealed by a pump and probe RDNMR study"-Poster presentation, September 4-6, 2013, 3rd Summer School on Semiconductor/Superconducting Quantum Coherence Effects and Quantum Information, Nasushiobara, Tochigi, **Japan**.

2. M. M. Uddin, H. W. Liu, K. F. Yang, K. Nagase, T. D. Mishima, M. B. Santos, and Y. Hirayama, "InSb Quantum Wells with Excellent Gate Controllability"-Oral presentation, JSAP Spring meeting, March 27-30, 2013, Kanagawa Institute of Technology, Kanagawa, **Japan**.

3. M. M. Uddin, H. W. Liu, K. F. Yang, K. Nagase, T. D. Mishima, M. B. Santos, and Y. Hirayama, "InSb Quantum Wells with Atomic Layer Deposited Gate Dielectrics"-Poster presentation, January 15-16, 2013, Tohoku-Harvard Joint Workshop (10th RIEC International Workshop on Spintronics), Sendai, **Japan**.

4. M. M. Uddin, H. W. Liu, K. F. Yang, K. Nagase, T. D. Mishima, M. B. Santos, and Y. Hirayama, "Magnetotransport Properties of InSb Two-Dimensional Electron Gas with Gate Dielectric Al_2O_3"-Oral presentation, September 11-14, 2012, JSAP Autumn meeting, Matsuyama University, Ehime, **Japan**.

5. M. M. Uddin, H. W. Liu, K. F. Yang, K. Nagase, T. D. Mishima, M. B. Santos, and Y. Hirayama, "Fabrication of a Gated InSb Quantum Well towards Pump-and-Probe Measurements of Nuclear-spin Polarization"-Poster presentation, September 5-7, 2012, 2nd Summer School on Semiconductor/Superconducting Quantum Coherence Effects and Quantum Information, Nasushiobara, Tochigi, **Japan**.

6. M. M. Uddin, H. W. Liu, K. F. Yang, K. Nagase, T. D. Mishima, M. B. Santos, and Y. Hirayama, "Effect of Gate Dielectric on Transport Properties of InSb Two-Dimensional Electron Gas"-Oral presentation, August 27-30, 2012, University of California, Santa Barbara, **USA**.

7. M. M. Uddin, H. W. Liu, K. F. Yang, T. D. Mishima, M. B. Santos, K. Nagase, and Y. Hirayama "Gate Controlled InSb Two-Dimensional Electron Gas and its Perspectives"-Poster presentation, International Workshop on Quantum Nanostructures and Nanoelectronics (QNN2011), October 3-4, 2011, University of Tokyo, Komaba, Tokyo, **Japan**.